

**Combined Structural and Compositional Modeling of  
Planetary Rings Due to Micrometeoroid  
Bombardment and Ballistic Transport**

Paul R. Estrada

Carl Sagan Center, SETI Institute

189 N. Bernardo Ave. # 100, Mountain View, CA 94043

Richard H. Durisen

Astronomy Department

University of Indiana, Bloomington, IN 47405

Jeffrey N. Cuzzi

NASA Ames Research Center

Mail Stop 245-3, Moffett Field, CA 94035

and

Demitri A. Morgan

USRA, NASA Ames Research Center

Mail Stop 245-3, Moffett Field, CA 94035

In internal review: July 5, 2012

?? manuscript pages, including...

?? Figures and ?? Tables and ?? Appendices

Proposed Running Title: "Modeling Structure and Composition"

Correspondence Address:

Paul R. Estrada

Carl Sagan Center, SETI Institute

189 N. Bernardo Ave. # 100, Mountain View, CA 94043

*E-mail:* Paul.R.Estrada@nasa.gov

*Phone:* (650) 810-0214

*FAX:* (650) 604-6779

## Abstract

We introduce a newly developed code for the modeling of structural and pollution evolution of Saturn’s rings, in tandem, due to the ballistic transport of micrometeorite impact ejecta. Previous work was restricted to the study of the exchange of mass and angular momentum, and material properties separately, but provided a solid framework for future development that could be advanced once we achieved a better understanding of key ring physical properties such as opacity, and improved processing power became available. Our result is a robust code capable of modeling both structural and compositional changes over time on both local and global scales...

## 1 Introduction

The rings’ huge surface area-to-mass ratio ensure that they are particularly susceptible effects of extrinsic meteoroid bombardment. Until recently, the mass of Saturn’s rings was thought to be on the order of a Mimas mass (although see Charnoz *et al.*, 2009). Indeed, directly comparing the ratio for Saturn’s rings to that of Mimas<sup>1</sup>, one finds that the rings’ surface area exceeds that of the latter by  $\sim 3 \times 10^4$ . A consequence of this is that hypervelocity micrometeoroid impacts on the rings, depending on the micrometeoroid flux (see below), likely erode them on timescales much shorter than their presumed age. Furthermore, these impacts can produce a large amount of particulate ejecta, the vast majority of which is ejected at speeds much less than the velocity needed to escape the rings. As a result, a copious exchange of ejecta between different ring regions can occur which can lead to changes

---

<sup>1</sup>For purpose of this illustration, all the mass is assumed to be in the B ring where the optical depth  $\tau \geq 1$ . The mass of Mimas is  $\sim 4 \times 10^{22}$  g.

in ring structure and composition on both local and global scales (Durisen *et al.*, 1989; Cuzzi and Estrada, 1998; Charnoz *et al.*, 2009). This process by which the rings evolve subsequent to meteoroid bombardment is referred to as “ballistic transport” of impact ejecta (Ip, 1983; Lissauer, 1984; Durisen, 1984a,b).

In a series of papers, Durisen and colleagues (Durisen *et al.*, 1989; 1992; 1996) developed the first rigorous dynamical code to model ring structural evolution due to meteoroid bombardment and ballistic transport and found that the influence of these processes on the rings could explain certain aspects of ring structure such as the fairly abrupt inner edges of the A and B rings, including the very similar “ramp” features which connect them to the Cassini division and C ring (see Figure 1), respectively given evolutionary times of  $\sim 100$  “gross erosion” times ( $\sim 10^8$  years). A gross erosion time  $t_G$  is defined as the time a reference ring annulus would disappear due to ejected material if nothing returned. In a complimentary study, Cuzzi and Estrada (1998) developed a model for the evolution of composition in which they calculated how both intrinsic and extrinsic non-icy materials build up over time and how these impurities are redistributed over the rings. Applying a radiative transfer model to the results of their “pollution transport” simulations, coupled with observations of the rings in three visible wavelengths (Estrada and Cuzzi, 1996; also see Estrada *et al.*, 2003), Estrada and Cuzzi found that they could simultaneously explain both the Cring/Cassini division versus A ring/B ring albedo and color dichotomy and the form and shape of the radial variation of color across the C ring/B ring transition on a similar timescale to Durisen and colleagues. A full review of previous work on the subject of ballistic transport can be found in Charnoz *et al.* (2009).

The impact ejecta mass *yield* from an extrinsic micrometeoroid collision with a ring particle that is not disrupted is thrown predominantly in the prograde orbital direction. This result arises naturally from consideration of impact geometries and probabilities which are azimuthally averaged over the rings (Cuzzi and Durisen, 1990). In addition to mass, ejecta carry away with them angular momentum. Since most of the ejecta from a non-disruptive (cratering) impact are prograde, they tend to reimpact the rings at outer locations where the specific angular momentum of ring material is larger. The net result is to decrease angular momentum at the secondary impact location leading to radial inward drift. On the other hand, an impact that leads to complete disruption of the target ring particle into several fragments would likely produce the opposite effect because it is reasonable to assume that such a catastrophic collision is more likely to result in a retrograde distribution with lower ejecta velocities than their prograde counterparts. In either case, the structure of the rings (*i.e.*, optical depth  $\tau$  and surface density  $\sigma$ ) will have an effect on the rate of material drift because the probability of ejecta absorption, which determines the actual mass that hits the rings as opposed to merely passing through them, not only depends on the azimuthally averaged angular aberrations over the orbit of the ring material, as well as weakly on the local  $\tau$ , but its angular momentum depends linearly on  $\sigma$  (Cuzzi and Durisen, 1990; Cuzzi and Estrada, 1998; Charnoz *et al.*, 2009).

Two key quantities that make it possible for their to be significant structural and compositional evolution of the rings over short and long timescales are the impact yield  $Y$  and the micrometeoroid flux  $\dot{\sigma}_e$ . Both  $Y$  and  $\dot{\sigma}_e$  are essential for providing more accurate age-dating of specific ring features, as well as the overall age of the rings themselves. The yield of a

single impact, which is defined as the ratio of ejecta mass to impactor mass, can be quite large depending on several factors (e.g., see Durisen, 1984b). The ejecta velocity distribution of an impact depends on the hardness of the target and the angle of impact (Cuzzi and Durisen, 1990). If the target is powdery, yields can be in excess of  $\sim 10^5 - 10^6$  for cratering (non-disruptive) impacts at normal incidence (e.g., Burns *et al.*, 1984), while micrometer-sized particles impacting into granular surfaces can have yields as small as  $\sim 10^3$  (Vedder, 1972). The ejecta velocities for the bulk material from cratering impacts tend to range from  $\sim 1 - 10 \text{ m s}^{-1}$ , much less than the escape velocity from the rings. This means that, regardless of whether impacts are cratering or disruptive (in this case the yield is effectively the entire target), one does not need to consider the net mass gain or loss from the rings due to micrometeoroid bombardment unless one considers very long exposure times (Charnoz *et al.*, 2009).

Past estimates of the current micrometeoroid flux (which likely was larger in the past) at Saturn vary slightly (e.g., Morfill *et al.*, 1983; Cuzzi and Estrada, 1998), but all suggest that the rings would be impacted by close to their own mass (for the Mimas mass estimate) over the age of the Solar System (Landgraf *et al.*, 2000). These estimates are largely based on the meteoroid mass fluxes measured by the Pioneer and Ulysses spacecraft between 5 – 10 AU (see, Cuzzi and Estrada, 1998, Fig. 17). Some hope for improving this estimate has recently surfaced from Galileo measurements of the flux at Jupiter. Sremčević *et al.* (2005) used an indirect technique to provide an estimate of the mass flux that may be at most off by a factor of 2 – 3 compared to previous estimates; however, the mass flux at Saturn has not yet been measured by Cassini allowing a similar study, and thus for now must continue

to remain uncertain.

For a given meteoroid flux and ring mass, micrometerite impacts on the rings will have two effects. First, as already pointed out above, they will lead to angular momentum loss within the rings. For example, it has been estimated that the C ring would be lost to the planet in  $\sim 10^7 - 10^8$  years (Cuzzi and Durisen, 1990) if no other mechanism were at work to sustain it. A similar age for the rings more closely related to ejected material was obtained by Northrop and Connerney (1987)<sup>2</sup>. Second, meteoroid material also darkens and “pollutes” the rings over time which also provides a powerful barometer for ring age. Doyle et al. (1989), and subsequently Cuzzi and Estrada (1998), using a mass flux from Morfill et al. (1983), noted that the relatively high albedo of the A and B rings was inconsistent with their having retained more than a small fraction of primitive, carbonaceous material they would have accreted over the age of the Solar System. Cuzzi and Estrada (1998) further demonstrated using their pollution transport model that the relatively small amount of extrinsic darkening material needed to evolve the inner B ring and the C ring to their current spectral color would also suggest a geologically young age for the C ring similar to the time it would take to lose the ring based on angular momentum loss arguments. This would seem to pose a problem for the possibility that the rings are more massive than previously thought, unless the C ring we see today is some great grand child of an original ancestor (Charnoz *et al.*, 2009).

In fact the C ring provides a fertile ground for ballistic transport modeling because, although most of the structure in the C ring remains unexplained, there are clear examples of

---

<sup>2</sup>It should be noted that resonant interactions with nearby ring-moons can also lead to significant angular momentum loss (e.g., Goldreich and Tremaine, 1982; Esposito, 1987; Poulet and Sicardy, 2001).

ballistic transport signatures to be seen. In **Figure 1**, we can see the sharp inner edge of the B ring that was found to be maintained by a balance between ballistic transport, which tends to sharpen low optical depth-to-high optical depth transitions, versus the broadening effect that results from viscous transport (Durisen *et al.*, 1992). Likewise, these workers also found, using a prograde ejecta distribution (Cuzzi and Durisen, 1990), that the adjoining ramp structure on the low optical depth side of the ring edge inevitably came about due to advective effects. Just as representative are the shapes of the C ring plateau peaks. Prograde ejected material leads in inward radial drift at the location where they land. Material drifts more quickly in low optical depth regions. This means that when a plateau is encountered with relatively higher optical depth, material will begin to “pile up”, which leads to a sharpening of the plateau outer edge as is observed in Figure 1. A region that is dominated by retrograde ejected material would exhibit outward radial drift, and thus sharpening of a plateau’s inner edge, which is also observed in Figure 1. Interestingly, there appears to be some symmetry about the ????? ringlet at around 87500 km. Whether this is coincidence or not is unclear. It may be that a combination of dominant C ring particle size, and impact velocities may lead to a transition between primarily cratering impacts versus impacts that are fragmentative (Estrada and Durisen, 2011).

Despite these clear examples of meteoroid bombardment and ballistic transport, the plateaus, as well as the undulating structure in the inner C ring which is not associated with any known resonances, remain enigmatic. How do these plateaus form and for how long do they persist? If the rings of Saturn are much more massive than previously thought, then high optical depth regions (*i.e.*, the B ring where most of this extra mass must be hidden

[e.g., Charnoz *et al.*, 2009]) should more easily be able to resist pollution from extrinsic bombarding material. A more massive rings does not necessarily indicate old rings, and indeed, the C ring is not long-lived. Yet, the most likely time that the main rings formed would have been at the Late Heavy Bombardment (LHB, ref?), setting up a mismatch between the age of the main rings, and the age of the C ring.

In this paper, we lay the ground work for more detailed, future modeling of micrometeoroid bombardment and ballistic transport in planetary rings with the introduction of new ballistic transport code that is capable of modeling both structure and composition in tandem that is able to model the rings over a broad range of spatial scales, and over both short and long timescales, and is robust enough that new physics can be readily incorporated into the code as it becomes available. In Section 2, we describe the development of our combined structural and compositional code. In Section 3, we present the results of demonstrative simulations, and finally in Section 4 we present our conclusions and discuss future work.

## **2 Combined Structural and Compositional Model**

### **2.1 Limitations of Previous Work**

Previous studies involving ballistic transport in Saturn’s main rings were limited on two fronts. From the structural standpoint, solving the ballistic transport equations (see Sec. 2.2.3) can be quite computationally expensive, even with today’s processing abilities. Ballistic transport essentially requires tracking the exchange of material from one location (radial bin) in the radial range of computation to every other radial location within its maximum

“throw distance”, which depends on the upper limit of the ejecta velocity distribution. Likewise, one must sum up all the contributions to that radial bin from all other radial locations whose ejecta can reach it. Because this involves integration over multiple variables (e.g., angles, velocities, deposition probabilities) at every time step over a potentially large histogram of radial bins, comprehensive parameter studies were unattractive, and global scale calculations intractable.

Another important handicap in previous studies was a lack of adequate data for some basic ring properties. For example, prior to Cassini, the ring surface density  $\sigma(R)$  had only been measured in several isolated spots, which were generally associated with spiral density wave regions. It was then only possible to determine the ring opacity  $\kappa(R) = \tau(R)/\sigma(R)$  in these discrete locations (e.g., Cuzzi *et al.*, 1984; Lissauer and Cuzzi, 1985). These estimates were then extended to non-density wave regions, assuming wave regions were not too different from non-wave regions (e.g., Cuzzi and Estrada, 1998). Because the ring particle size distribution is well approximated by a power law  $n(r) \propto r^{-3}$  (where  $r$  is the ring particle radius) in most regions (e.g., Zebker *et al.*, 1985), the opacity depends primarily on the largest particle size. With these assumptions, Cuzzi and Estrada (1998) utilized the variance technique of Showalter and Nicholson (1990) to determine the largest effective radius particle from the Voyager stellar occultation data across a range of ring radii where no spiral density waves existed. Ultimately, the former authors could only estimate the spatial variability of  $\kappa$  because of a lack of occultation data in optically thick regions. The simulations of Durisen *et al.* adopted the condition  $\tau = \sigma$  and thus the opacity was assumed to be a constant value dependent on some reference value of  $\sigma$  (e.g.,  $\sigma = 96 \text{ g cm}^{-2}$

for  $\tau = 1$  in the inner B ring, see Cuzzi *et al.*, 1984).

A major limitation of the C ring/inner B ring compositional study of Cuzzi and Estrada (1998) was the assumption that the underlying ring structure could be kept constant while the ring composition evolved. These authors assumed this because Durisen *et al.* (1992) had found in their structural evolution simulations that constant optical depth regions and inner sharp edges can remain more or less unchanged over long timescales. As a result, Cuzzi and Estrada assume that the optical depth and mass surface density were time-independent on the timescale of compositional evolution. This meant that the cumbersome loss and gain integrals (see Sec. 2.2.4) that determine the redistribution of mass and angular momentum due to ballistic transport (which depend on  $\tau$ ) needed only to be done once. At the time this represented a considerable savings in computational time, but prevented these authors from discerning, for example, “transient” compositional properties on smaller timescales that might arise from the structural evolution of material. As we will show in this paper, transient structures occur quite readily on relatively short timescales.

Cassini observations is allowing for a more detailed understanding of dynamical ring properties such as the opacity, surface density, and optical depth which are key quantities in modeling of ring structure. In particular, analysis of spiral density waves in the rings suggest that the rings are composed of virtually opaque clumps separated by nearly transparent gaps which will have consequences for both ring opacity (Sec. 2.2.5) and viscosity (Sec. 2.2.6). As cassini data continues to be analyzed, we fully expect to integrate these new findings as they become available to improve our modeling in the future.

## 2.2 The Ballistic Transport Code

The ballistic transport code (hereafter BT code) evolves the surface mass density of the rings  $\sigma(R, t)$  over time, and thus its *structure*, by solving the system of equations given below in Sec. 2.2.3. The code further tracks the changes in the fractional mass of extrinsic (bombarding) material, or pollutant which is assumed to be made up of some fraction of icy and non-icy constituents, and the rings' intrinsic material which is assumed to be composed mostly of water ice mixed with a very small fraction of absorbing material which is different from the micrometeorite impactors. Thus the BT code also simultaneously evolves the bulk *composition* of the rings.

In ballistic transport, the two main effects that contribute to the rings' evolution are the direct net mass exchange of micrometeoroid impact ejecta between different ring regions (Ip, 1983), and the differential radial drift of material due to the direct net angular momentum exchange that comes as a result of the redistribution of impact ejecta (Lissauer, 1984). Secondary effects that are related to the direct deposition of extrinsic material and its redistribution can also play a role, but are lesser in magnitude and more relevant over long timescales (Durisen *et al.*, 1996).

The exchanges in mass and angular momentum are determined at any radial location  $R$  in a Lagrangian (*i.e.*, unequally spaced) radial grid by computing (1) the local gain rate in mass and angular momentum by accounting for all of the incoming ejecta from neighboring ring regions that are absorbed at  $R$ ; and, (2) the local loss rate by accounting for the all of the ejecta created at  $R$ , which are ejected at different speeds and in different directions, that are absorbed at radial locations different from  $R$ . The net exchanges at a given  $R$  are then

determined by differencing the local gains and losses. Advection further modifies the local surface mass density through the compression or expansion of the Lagrangian cells, while viscous angular momentum transport provides an additional source of radial drift.

In this section we describe the motivation and mathematical formulation for the BT code. Much of what is presented below has been described elsewhere in detail (e.g., Durisen *et al.*, 1989; 1992; 1996; Cuzzi and Estrada, 1998); however, given the mathematical and numerical focus of this paper, we believe it is justified to repeat some of these previous descriptions while emphasizing differences in approach and new physics when appropriate.

### **2.2.1 The impact flux on the rings and definition of the gross erosion time**

Of the various input parameters for the modeling of ballistic transport in Saturn’s rings, the micrometeroid flux remains the most fundamental. For this work, we continue to use the value of the one-sided, incident flux at infinity  $\dot{\sigma}_{\infty} = 4.5 \times 10^{-17} \text{ g cm}^{-2} \text{ s}^{-1}$  used in Cuzzi and Estrada (1998) initially obtained from direct integration over the 1 AU interplanetary flux models of Grün *et al.* (1985) and Ip (1984) which was used by Cuzzi and Durisen (1990), and subsequently by Durisen and colleagues in later papers. However, the value then was arrived at based on a mistaken assertion. Cuzzi and Estrada (1998) reanalyzed and corrected the estimates from Cuzzi and Durisen (1990) by including Pioneer 10/11 and Ulysses spacecraft data (see Fig. 17, Cuzzi and Estrada, 1998). These authors found that the previously assumed value for  $\dot{\sigma}_{\infty}$  remained plausible within a factor of 2 – 3, but for different reasons than found by previous workers (see Cuzzi and Estrada, 1998 for a detailed discussion).

The two-sided flux of micrometeorites impacting the ring plane at some radial location  $R$  is given by

$$\dot{\sigma}_{\text{im}} = 2\dot{\sigma}_{\infty}\mathcal{A}(\tau)F_{\text{G}}(R/R_0)^{-0.8}, \quad (1)$$

where we have accounted for the gravitational focusing of the planet using an asymptotic relative velocity of  $14 \text{ km s}^{-1}$ , which is numerically averaged into a factor  $F_{\text{G}} = 3$  at a reference radius  $R_0 = 1.8 R_{\text{S}}$  ( $R_{\text{S}} = 60330 \text{ km}$  is the equitorial radius of Saturn). The flux at other radii are obtained by the numerical fit  $(R/R_0)^{-0.8}$  to the radial dependence of the calculated focusing (Durisen *et al.*, 1992). The optical depth dependent function

$$\mathcal{A}(\tau) = [1 - e^{-(\tau/\tau_s)^p}]^{1/p}, \quad (2)$$

is a parameterization of a numerically determined impact probability that depends on  $\tau$  and the various angular aberrations averaged over the orbit of the ring particles (Cuzzi and Durisen, 1990). Here the fit parameters  $\tau_s = 0.515$  and  $p = 1.0335$ .

The actual mass flux of ejected material at reference radius  $R_0$  is determined by integration over the full ejecta yield function  $\mathcal{Y}$  derived by Cuzzi and Durisen (1990)

$$\dot{\sigma}_{\text{ej}}(R_0) = 2\dot{\sigma}_{\infty} \left( \frac{Y}{Y_0} \right) \int_x \int_{\Omega} \mathcal{Y}(R_0, x, \Omega) dx d\Omega \approx Y \dot{\sigma}_{\text{im}}(R_0), \quad (3)$$

which depends on ratio of the ejecta to orbital velocities  $x = v_{\text{ej}}/v_K$ , and solid angle  $\Omega$ . The ejecta distribution function  $\mathcal{Y}$  contains all the information about impact and escape probabilities, gravitational focusing, and is normalized to a yield of  $Y_0 = 10^4$  at  $14 \text{ km s}^{-1}$

impact velocity (Lange and Ahrens, 1987). The approximation on the RHS of Eq. (3) is off by a factor of  $\sim 1.2$  to the exact calculation obtained through direct integration of  $\mathcal{Y}$  (Cuzzi and Estrada, 1998) which we always utilize in the BT code, but we may often use it for illustrative purposes.

We can now define the ‘gross erosion time’  $t_G$  as the fundamental time unit of ballistic transport

$$t_G = \frac{\sigma}{\dot{\sigma}_{ej}} \approx \frac{\sigma}{Y\dot{\sigma}_{im}}. \quad (4)$$

The gross erosion time is defined as the time it would take for a ringlet of surface density  $\sigma$  to be completely eroded away if no material returned. For example, using the two-sided, gravitationally focused mass flux in Eq. (1) and an ejecta yield of  $Y = 10^4$ , a reference ring annulus with  $\sigma = 100 \text{ g cm}^{-2}$  would erode away in  $t_G \sim 10^6 - 10^7$  years.

We normalize the time units of the BT code to the gross erosion time which allows our simulations to be independent of specific values of the micrometeoroid flux. However, the actual ages derived from our simulations remain quite uncertain because the absolute timescale for ring erosion depends on the typical impact yields of ejecta (which depend on the hardness of the target), and the efficiency with which extrinsic bombarding material retains its absorptive properties in addition to the weakly constrained micrometeoroid flux at Saturn.

### 2.2.2 Code assumptions

The Saturnian rings are modeled as a Keplerian thin disk which is axially symmetric, with Saturn taken to be a point mass, and ring self-gravity is ignored. A thin disk is a more than reasonable assumption because the velocity dispersion  $c$  of ring particles typically have magnitudes of a few millimeters per second (Cuzzi *et al.*, 1984) somewhat akin to the escape velocity from several-meter-sized particles which are the sizes we consider to be the upper bound in our assumed particle size distribution. On the other hand, the orbital speeds of ring particles  $v_K$  are on the order of tens of kilometers per second. The random motions due to  $c$  lead to a vertical thickness  $H/R \sim c/v_K \ll 1$ , or an  $H$  of a few times our largest particle size.

To consider the disk to be thin with respect to ballistic transport, the radial and vertical excursions of impact ejecta should be much greater than  $H$ . This is easy to see by comparing typical ejecta velocities to  $c$ . Ejecta velocities  $v_{ej}$  from non-disruptive impacts can vary from  $\sim 1 - 100 \text{ m s}^{-1}$  depending on the hardness of the target (e.g., Lange and Ahrens, 1982; Hartmann, 1985). The inward or outward radial excursion of an ejecta particle, which we refer to as its ‘throw distance’, is given by  $|\delta R| \approx 4xR$  (Morfill *et al.*, 1983; Durisen *et al.*, 1992). Comparing the radial throw distance to the ring vertical thickness,  $|\delta R|/H \sim 4xR/R(c/v_K) \sim 4v_{ej}/c \gg 1$ . By the same token, the average vertical excursion is  $|\delta z| \sim v_{ej}P/2 \sim \pi R(v_{ej}/v_K)$  so that again we find  $|\delta z|/H \sim \pi v_{ej}/c \gg 1$ .

Our assumption of axial symmetry stems from a comparison of timescales. The typical orbital period of a ring particle is on the order of tens of hours whereas the relevant timescales of ballistic transport are on the order of  $t_G \sim 10^5 - 10^7$  years. Given this disparity, it

is reasonable to expect that transient deviations from axial symmetry in underlying ring structure average out over our the timescales involved in our simulations. We use a variable timestep in our BT code (Sec. 2.3.3) which could be as short as a few years if the ring ambient conditions in the simulation call for it. This still equates to  $\lesssim 10^3$  orbits which should not invalidate our assumption. We leave consideration of the much more complicated problem of 2-D ballistic transport modeling for future study.

Ring self-gravity is considered to be unimportant with respect to impact ejecta because the escape velocity from the ring particle size that dominates the ring mass (a few meters) is much smaller than the typical ejection speeds we use here. The presence of larger moonlets whose masses are large enough to produce escape velocities on the same order as that of the typical ejectum are also not considered as important as these objects are sparse and thus would only effect a very small fraction of ejecta at any given time. With regards to treating Saturn as a point mass, this is justified based on timescale arguments. Saturn's non-sphericity can lead to nodal precession and apsidal motion on a timescales of tens of days in the C ring, with timescales increasing with radial location (Lissauer and Cuzzi, 1982). Given the relatively short orbital times of ring particles, ejecta are expected to at most complete a few orbits before being reabsorbed (Durisen *et al.*, 1989; Cuzzi and Durisen, 1990). Thus, Saturn's oblateness should make no difference for particle trajectories.

We assume that all ejecta travel on Keplerian elliptical orbits between their point of ejection and their point of eventual reabsorption, and reabsorbed ejecta do not produce secondary ejecta distributions. The former assertion is valid from comparison of the typical ejecta velocities to the local Keplerian orbital velocity. Because  $v_{ej}/v_K \ll 1$ , the ejecta

travel on slightly elliptical orbits and cannot escape the system, but rather reimpact the ring at distances up to the maximum throw distance  $\sim 4x_{\max}R$ . The latter assertion seems sensible in that the secondary impacts of ejecta grains with the regoliths of ring particles would be at up to  $\sim 100 \text{ m s}^{-1}$  velocities are likely to be highly inelastic (e.g., Hartmann, 1985; NEWER REFS??). The secondary ejecta velocities are expected to be  $\ll v_{\text{ej}}$  and thus the radial excursions are expected to be very small with reimpacts occurring within the maximum radial bin resolution we use in the BT code ( $\gtrsim$  a few kilometers).

A radiative transfer analog which assumes plane-parallel symmetry is used to compute the ejecta distribution functions  $\mathcal{Y}$  (Cuzzi and Durisen, 1990) which are used to calculate the probabilities that incoming micrometerites, or subsequent incoming or outgoing ejecta will impact a ring particle as they pass through the rings. The ejecta distribution is direction-dependent and calculates the total rate of impact ejecta emission or absorption per unit area for a given local ring region of surface mass density  $\sigma$  and optical depth  $\tau$ . Furthermore, the distribution function assumes that impacts are cratering and non-disruptive (see Sec. 2.2.7).

We assume the particle size distribution in the rings to be the same everywhere and at all times with lower and upper cutoffs  $r_1, r_2$  of 3 cm and 3 m, respectively. For our current modeling efforts, this may be a prudent assumption given that the ring particle size distribution is well approximated by a power law in particle radius  $r$  of  $n(r) \propto r^{-3}$  in most regions (e.g., Zebker et al. 1985). This presumes that some local processes act to maintain the distribution in spite of the slow losses or gains that are attributable to ballistic transport. Indeed, the details of the size distribution should be unimportant if the typical impacts are, as we assume in this paper, cratering and thus leave the target particle intact.

Under these circumstances, the particle erosion rate only depends on the impact velocity and micrometeorite influx rate (e.g., Morfill *et al.*, 1983; Durisen *et al.*, 1989). If micrometeoroid impacts were significantly disruptive (leading to catastrophic break-up), our assumption of constant  $r(R, t)$  would likely need to be re-evaluated (see Sec. 2.2.7). The range in size of the micrometeoroid flux is assumed to be  $1 \lesssim r_{\text{im}} \lesssim 100 \mu\text{m}$  (Cuzzi and Estrada, 1998). Incidentally, this means that radiation and electromagnetic forces have little if any consequences for the trajectories of ejecta particles which are assumed to be  $r_{\text{ej}} \gtrsim r_{\text{im}}$  (see Durisen *et al.*, 1989 for a discussion).

The intrinsic composition of the rings is assumed to be primarily water-ice with a small fraction of spectrally red, absorbing material that is intimately mixed within the ice matrix. Cuzzi and Estrada (2008) found that Titan tholins provided a good fit to the observations, however other candidates for the absorbing material have been proposed (e.g., Clark *et al.*, 2012). The extrinsic, bombarding material is assumed to be composed of a fraction of a spectrally neutral, darkening agent, and water ice. We typically choose this fraction  $f_{\text{ext}} \sim 0.5$ . The BT code tracks the mass fraction  $f_e(R, t)$  of extrinsic material and assumes that the remainder  $(1 - f_e)$  is the admixture of primordial material. Impacting material is assumed to be retained locally in the ring with an efficiency  $\eta$ , and uniformly mixed throughout the local mass density  $\sigma(R, t)$ . Thus, all the components of composition are viewed to be volumetrically mixed within the ring particles at all times.

This assumption is more than likely adequate over long timescales ( $>$  a few  $t_G$ ). However, more recent work that models regolith growth in ring particles due to micrometeoroid bombardment suggests that, for ring particles that initially begin as icy bodies, their re-

regoliths remain more or less constant in the fractional amount of pollutant for timescales  $\lesssim t_G$  (Elliott and Esposito, 2011). Once the regolith has fully developed, fractional mass increases linearly with time which is consistent with this work. The work of Elliott and Esposito (2011) becomes particularly relevant when considering the study of shorter timescale, transient features. For example, a recent local event such as the breakup of a small icy moon may lead to the resetting, locally, of the ballistic transport “clock”, an idea that has already been suggested to explain variations in brightness in the rings over length scales of  $\sim 1000 - 3000$  km that do not seem consistent with ballistic transport acting over long timescales (Esposito *et al.*, 2005). In future work, we plan to incorporate these effects into our BT code.

Finally, as has been stated previously (Durisen *et al.*, 1989), the ballistic transport equations (Sec. 2.2.3) account for conservation of mass and angular momentum, but not for energy. The reason is that micrometeoroid impacts play little if any role in maintaining the velocity dispersion in the rings against damping due to collisions as most of the kinetic energy of the impactors and ejecta are dissipated in relatively short order. To see this, we consider the impact of a particle of mass  $m_{\text{im}}$  with a ring particle of mass  $m_p$ . Through momentum exchange arguments, the random velocity imparted to a ring particle  $m_p$  through the impact with a particle  $m_{\text{im}}$  is  $\Delta v \sim \mu_m v_{\text{im}} \sim Y \mu_m v_{\text{ej}}$ , where  $\mu_m$  is the reduced mass. The ring particle  $m_p$  is impacted once every

$$t_{\text{im}} \approx \frac{m_{\text{im}} \sigma}{m_p \dot{\sigma}_{\text{im}}} \approx \mu_m \frac{\sigma}{\dot{\sigma}_{\text{im}}} = (\mu_m Y) t_G. \quad (5)$$

The rate then at which energy is introduced into the system as a result of these impacts is

$\Delta v^2/t_{\text{im}}$  which can be compared with the rate at which energy is dissipated due to inelastic collisions (Cuzzi *et al.*, 1979)

$$\frac{\Delta v^2}{t_{\text{im}}} = \mu_{\text{m}} Y \frac{v_{\text{ej}}^2}{t_{\text{G}}} \gtrsim \frac{c^2 \tau \Omega (1 - \epsilon^2)}{3\pi} \quad \rightarrow \quad \mu_{\text{m}} \gtrsim 1.25 \times 10^{-12} \frac{c^2 \sigma \tau (1 - \epsilon^2)}{x^2}. \quad (6)$$

here,  $c$  is the velocity dispersion in the rings,  $\epsilon$  is the coefficient of restitution and  $x$  is the ratio of impact to Keplerian orbital velocity. In our modeling, we implicitly assume a ring particle size distribution  $n(r) \propto r^{-3}$  with an upper size cutoff of  $r_p = 3$  m. using this as the size for  $m_p$  and  $c \sim 0.2$  cm s<sup>-1</sup>, we consider typical values for our simulations for a C ring plateau with  $\tau = 0.4$ ,  $\sigma = 40$  g cm<sup>-3</sup> and  $x = 10^{-3}$  one finds that  $m_{\text{im}} \gtrsim 3(1 - \epsilon^2)$  cm. The mass peak in the interplanetary micrometeorite flux, which is presumed to be cometary in origin, is around 100  $\mu\text{m}$  (e.g., Grün *et al.*, 1985; Cuzzi and Estrada, 1998), while Edgeworth-Kuiper belt dust particles have a mass peak between 1 – 10  $\mu\text{m}$  (Poppe *et al.*, 2010; Poppe and Horányi, 2012). Although ring particle collisions are highly inelastic, coefficients of restitution very close to unity would be needed for impacts by meteorites to be able to maintain the observed velocity dispersion in the rings. Thus we assume that the velocity dispersion in the rings is maintained by some other process which we do not model and, as a consequence, we do not consider conservation of energy in our system of equations (Sec. 2.2.3).

### 2.2.3 Working equations

We define the ring system to be thin, and azimuthally symmetric so that the only spatial variable is the ring semimajor axis  $R$  centered on the planet. Given our set of assumptions

from Sec. 2.2.2, the ring system is described at time any time  $t$  by a surface mass density  $\sigma(R, t)$  and normal optical depth  $\tau(R, t)$ , where the two quantities are related through the ring opacity  $\kappa(R, t) = \tau/\sigma$ . The opacity may explicitly or implicitly incorporate information about the ring particle density  $\rho_p$ , and size distribution assumed.

The evolution of the ring system under ballistic transport with time is determined through solving the following set of equations. The mass continuity equation

$$\frac{\partial \sigma}{\partial t} + \frac{1}{R} \frac{\partial}{\partial R} (\sigma R v_r) = \Gamma_m - \Lambda_m + \dot{\sigma}_{\text{im}}, \quad (7)$$

or, alternatively the areal angular momentum density continuity equation

$$\frac{\partial}{\partial t} (\sigma R v_\theta) + \frac{1}{R} \frac{\partial}{\partial R} [R (\sigma R v_\theta v_r)] = \Gamma_h - \Lambda_h + \dot{\sigma}_{\text{im}} R v_\theta, \quad (8)$$

follows the local changes in  $\sigma$  and  $R$  due to the net loss or gain of ejecta to and from neighboring ring regions. The RHS of Eq. (7) accounts for the direct mass gains  $\Gamma_m$  and losses  $\Lambda_m$  by integrating the ejecta distributions over the rings taking into account cylindrical effects, while the RHS of Eq. (8) where  $v_\theta = v_K$  is the local Kepler velocity are the angular momentum loss and gains (see Sec. 2.2.4). The term  $\dot{\sigma}_{\text{im}}$  is the impact flux of micrometeorites on the rings. The divergence of the mass flux caused by the slow radial drift of ring material brought on by angular momentum transport are accounted for in the 2nd term on the LHS of (7). The total radial drift velocity  $v_r$  can have multiple components. Primary is that due to the ballistic transport mechanism itself

$$v_r^{\text{ball}} = \left( \sigma \frac{dh_c}{dR} \right)^{-1} [\Gamma_h - \Lambda_h - h_c(\Gamma_m - \Lambda_m)], \quad (9)$$

which can readily be derived from combining Eqns. (7) and (8) for the inviscid case. In (9),  $h_c = Rv_K = (GMR)^{1/2}$  is the specific angular momentum for circular motion with  $G$  the gravitational constant, and  $M$  the mass of the planet. A second component to radial drift is due to the viscous angular momentum transport

$$v_r^{\text{visc}} = -\frac{3}{\sigma h_c} \frac{\partial}{\partial R} (h_c \sigma \nu), \quad (10)$$

where  $\nu(R, t)$  is the kinematic viscosity (Sec. 2.2.6). Additional contributions to the radial drift of material that are due to the collective effects of meteoroids such as mass loading and/or loss of ejecta angular momentum  $v_r^{\text{masl}}$ , and torques caused by asymmetric absorption of meteoroid ejecta  $v_r^{\text{torq}}$  (Durisen *et al.*, 1996) are also included in the calculation of the total  $v_r$  though these effects are secondary, and are more important over long simulations (see Sec. 2.2.8).

Changes in the composition of the rings is followed using the equations for the evolution of the surface mass density of the extrinsic and intrinsic components

$$\frac{\partial \sigma_e}{\partial t} = \eta f_{\text{ext}} \dot{\sigma}_{\text{im}} + \Gamma_{\text{m,e}} - f_e(r, t) \Lambda_m - \frac{1}{R} \frac{\partial}{\partial R} (\sigma_e R v_r), \quad (11)$$

$$\frac{\partial \sigma_i}{\partial t} = (1 - \eta f_{\text{ext}}) \dot{\sigma}_{\text{im}} + \Gamma_{\text{m,i}} - [1 - f_e(r, t)] \Lambda_m - \frac{1}{R} \frac{\partial}{\partial R} (\sigma_i R v_r), \quad (12)$$

where the parameter  $f_{\text{ext}}$  is the non-icy fraction of a micrometeoroid impactor, and  $\eta$  is

the efficiency at which the impacting material retains its absorptive properties (Cuzzi and Estrada, 1998). The gain integrals  $\Gamma_{m,e}$  and  $\Gamma_{m,i}$  are described in the next section.

#### 2.2.4 Computation of losses and gains

The essence of the ballistic transport process lies in the changes in the local mass surface density due to the differences between losses and gains of ejecta material at some  $R$ , which is of order  $\sim x$  away from sharp edges, and  $\sim x^2$  at sharp edges, and the order  $\sim x^2$  differences between the radial velocities  $v_r$  between neighboring ring regions through the divergence term. Quite literally ballistic transport depends on differences of small differences between losses and gains (Durisen *et al.*, 1989). The losses  $\Lambda$  and gains  $\Gamma$  in mass and angular momentum per unit area per unit time must be computed every time step, and at each radial location within the ring. The losses in mass and angular momentum must account for the total rate at which material (and their associated angular momenta) at ring radius  $R$  is being ejected in all possible directions and at all possible speeds to other locations  $R'$  where the ejecta are reabsorbed:

$$\Lambda_m = \mathcal{R}(R, \tau) \int_0^\infty dx \int_0^{2\pi} d\phi \int_{-1}^1 \mathcal{P}(R, R') f(x, \theta, \phi) d \cos \theta, \quad (13)$$

$$\Lambda_h = h_c \mathcal{R}(R, \tau) \int_0^\infty dx \int_0^{2\pi} d\phi \int_{-1}^1 (1 + x \cos \theta) \mathcal{P}(R, R') f(x, \theta, \phi) d \cos \theta. \quad (14)$$

Here,  $\mathcal{R}$  gives the total rate of mass ejection at radius  $R$  per unit area, and  $\theta$  and  $\phi$  are the angles between the ejecta velocity vector and the unit vector tangent to the ring particle's orbit, and the angle made by projection of the ejecta velocity vector onto the plane defined by

the radial unit vector (pointing away from the planet) and the ring plane normal, respectively.

The function  $f$  specifies the distribution of ejecta that escapes  $R$  over velocity and solid angle defined by  $\theta$  and  $\phi$ . By definition then, the integral  $\iiint f(x, \theta, \phi) dx d\phi d\cos\theta \equiv 1$ .

The probability function  $\mathcal{P}$  is given by Eq. (30) of Durisen et al. (1989)

$$\mathcal{P}(R, R') = \frac{1 - e^{-\tau'_z}}{1 - e^{-(\tau_z + \tau'_z)}}, \quad (15)$$

where  $\tau_z$  and  $\tau'_z$  are the optical depths as measured from the angles of incidence relative to the ring normal at  $R$  and  $R'$ , respectively (Eq. [29], Durisen *et al.*, 1989). Equation (15) gives the total probability that the ejected particle will be absorbed at  $R'$  rather than at  $R$ .

The corresponding gains in mass and angular momentum per unit area per unit time at the radial location  $R$  are calculated through the integrals  $\Gamma_m$  and  $\Gamma_h$  which account for all the ejecta from neighboring ring regions  $R'$  that can reach  $R$ . Because ballistic transport depends on the small net differences between the losses and gains, Durisen et al. (1989) argued that the gain integrals should be as closely analogous to Eqns. (13) and (14) as possible for purposes of numerical accuracy. This was accomplished by relating the radius of ejection  $R$  to all possible radii of absorption  $R'$  by deriving a mathematical description of the Keplerian elliptical orbit followed by the ejectum  $R' = RA(x, \theta, \phi)$ , where the function  $A$  is given by Eq. (33) of Durisen et al., (1996). Summing up all of the contributions to the ring annulus  $2\pi R dR$  from annuli  $2\pi R' dR'$  then leads to the expressions for the mass and angular momentum gain integrals

$$\Gamma_m = \int_0^\infty dx \int_0^{2\pi} d\phi \int_{-1}^1 \mathcal{R}(R', \tau') A^2 \mathcal{P}(R', R) f'(x, \theta, \phi) d\cos\theta, \quad (16)$$

$$\Gamma_h = \int_0^\infty dx \int_0^{2\pi} d\phi \int_{-1}^1 h'_c(1 + x \cos \theta) \mathcal{R}(R', \tau') A^2 \mathcal{P}(R', R) f'(x, \theta, \phi) d \cos \theta, \quad (17)$$

where evaluation of quantities is at the location  $R'$  which is itself evaluated in terms of  $x$ ,  $\theta$  and  $\phi$ . The fractional mass gain integrals  $\Gamma_{m,e}$  and  $\Gamma_{m,i}$  incorporate the mass fractions of extrinsic and intrinsic materials, but are nonetheless similar to Eq. (16)

$$\Gamma_{m,e} = \int_0^\infty dx \int_0^{2\pi} d\phi \int_{-1}^1 f_e(R', t) \mathcal{R}(R', \tau') A^2 \mathcal{P}(R', R) f'(x, \theta, \phi) d \cos \theta, \quad (18)$$

with an analogous expression for  $\Gamma_{m,i}$  by simply replacing  $f_e(R', t)$  with  $1 - f_e(R', t)$ . In Section 2.3.4 we describe our technique for solving these integrals numerically.

With regards to the particle size distribution in the rings, Durisen et al., (1989) originally employed two different assumptions about  $n(r)$  in the hopes that they might bracket the true particle behavior within the rings. The first was to assume that all ring particles are the same size at any given distance  $R$ , but can differ in particle radius  $r(R)$ . This led to an additional continuity equation in terms of particle number density. The second assumption, which Durisen and colleagues exclusively employed in later papers, and what we assume here is that of the same  $n(r)$  at all  $R$ . The primary reason at the time for not modeling a particle size distribution was computational as it meant that an additional integration parameter would be introduced in the losses and gains above. With improved computational ability (including the fact that the BT code is parallelized, Sec. 2.3.4), as well as continuing improvements in our understanding of processes that affect the evolution of ring particle size in the rings such as particle-to-particle collisions (REFS), and disruptive impacts (REFS) such an endeavor is certainly possible. In future work in particular, we plan to include disruptive impacts (see

Sec. 2.2.7) and thus will include these physics at a later time.

### 2.2.5 Ring Opacity Models

Prior to Cassini, the surface mass density  $\sigma$  had only been measured in several isolated spots, which were generally associated with spiral density wave regions. Knowing both the surface mass density and the optical depth allows one to calculate the ring opacity  $\kappa = \tau/\sigma$ . In the work of Cuzzi and Estrada (1998), in which they investigated whether pollution transport alone could explain the detailed shape of the ring color profiles across the rings, only two such locations were known in C ring: the Maxwell ringlet; and, the Janus 2:1 density wave. In order to achieve their goal, these authors required an opacity profile with higher radial resolution<sup>3</sup>. Given that the ring particle size distribution is best described by a power law in most regions (see Sec. 2.2.2; Zebker *et al.*, 1985),  $\kappa$  depends primarily on the largest particle size. Under this assumption, Cuzzi and Estrada (1998, see their Fig. 5) utilized the variance technique of Showalter and Nicholson (1990), which determines the largest “particle” size with high radial resolution to determine from the  $\delta$ -Sco Voyager stellar occultation the largest effective radius particle  $r_{\text{eff}}$  across a range of ring radii where no spiral density waves existed. The scatter in their derived  $\kappa$  values, particularly coupled with values inferred by others, led these authors to adopt very simple  $\kappa(R)$  profiles:

---

<sup>3</sup>In contrast,  $\kappa$  never explicitly appears in the simulations of Durisen and colleagues. Rather, these workers normalize  $\sigma$  such that  $\sigma(\tau = 1) = 96 \text{ g cm}^{-2}$  so that  $\kappa \approx 0.01 \text{ cm}^2 \text{ g}^{-1}$  everywhere in the rings (Durisen *et al.*, 1992; 1996).

$$\kappa(R) = \begin{cases} \kappa_1 & R \leq R_1; \\ \kappa_1 - \frac{\kappa_1 - \kappa_2}{R_2 - R_1}(R - R_1) & R_1 < R < R_2; \\ \kappa_2 & R \geq R_2. \end{cases} \quad (19)$$

where  $\kappa_1 = 0.05$ ,  $\kappa_2 = 0.009$ ,  $R_1 = 1.5 R_S$  (roughly the base of the C ring ramp, see Fig. 1), and  $R_2$  was modestly varied to different locations in the very inner B ring. The estimated  $\kappa = \kappa_2$  for the B ring opacity was actually an average over a range of possible values, due to its uncertainty as a result of a lack of occultation data in optically thick regions (see Fig. 11 of Showalter and Nicholson 1990).

The  $\sim 100$  spiral density waves analyzed by Cassini UVIS and VIMS (e.g., Colwell *et al.*, 2007; Hedman *et al.*, 2007; Nicholson *et al.*, 2008) have greatly improved our knowledge of key ring dynamical properties such as the optical depth and mass surface density. For example, these workers find the rings are composed of virtually opaque clumps separated by nearly transparent gaps. These observations have been attributed to self-gravity wakes which have been shown numerically (using local  $N$ -body simulations) to spontaneously form as a result of the combined effects of self-gravity and collisional damping of particles (e.g., Salo 1995; Daisaka and Ida 1999; Ohtsuki and Emori 2000). Nicholson *et al.* (2008) and Colwell *et al.* (2008) have exploited this apparent variation to separate the (large and unconstrained)  $\tau$  within the wakes from the  $\tau$  and fractional area of the nearly transparent gaps. These workers find that for (VIMS) occultations spanning both the A and B rings ( $11^\circ < B < 51^\circ$ ), gap optical depths are relatively constant ( $0.15 < \tau < 0.3$ ) wherever wakes exist. Moreover, these wakes have a nonaxisymmetric structure which must eventually be accounted for in

our ejecta probability distributions as well as radiative transfer modeling of composition of the rings and its constituent materials (see Sec. 4).

Analysis of these extensive observations (which also gives the typical pitch angle, height and spacing to width ratios of the dense wake clumps, e.g., Colwell *et al.*, 2006; 2007) allows one to determine an “autocorrelation length scale” which characterizes the physical dimensions of contiguous physical material (clumps) blocking the starlight. This scale varies depending on the viewing geometry, because the clumps are not spherical, thus complicating the search for an “effective largest particle size” that characterizes the ring opacity  $\kappa$ . However, by combining results from multiple Cassini UVIS stellar occultations that encompass a broad range of viewing geometries, the goal is to be able to constrain the absolute physical dimensions of the self-gravity wakes (Colwell, priv. comm.).

One observation that Cuzzi and Estrada (1998) gleaned from point-by-point inspection of their derived opacity values in the C ring was that these values indicated a preferential association of low  $\kappa$  with relatively higher optical depths plateaus, while higher  $\kappa$  were associated with regions away from plateaus where  $\tau$  was lower. This was somewhat supported by comparison, at the time, with Voyager visual and radio wavelength optical depths. If true, this effectively would say that there is more mass in the plateaus than the simple model in Eq. (19) would predict. This possibility suggests an alternative model for the ring opacity that we utilize for this work, namely that the opacity depends on  $\tau$  (or alternatively,  $\sigma$ ). For models that explore the C ring and inner B ring, we can define the initial values of the opacity  $\kappa(R, 0) = a + b/\tau(R, 0)$ , and at all later times through

$$\kappa(R, t) = \frac{a}{2} + \frac{a}{2} \left[ 1 + \frac{4b}{a^2 \sigma(R, t)} \right]^{1/2}, \quad (20)$$

where the fit parameters  $a = \kappa_1 + (\Delta\kappa/\Delta\tau)\tau_2$ ,  $b = -(\Delta\kappa/\Delta\tau)\tau_1\tau_2$ ,  $\Delta\kappa = \kappa_2 - \kappa_1$  and  $\Delta\tau = \tau_2 - \tau_1$ . The choices for the  $\kappa_{1,2}$  and  $\tau_{1,2}$  can readily be chosen to be consistent with the profile given in Eq. (19).

The above formula is heuristic and is simply meant to allow us to associate a certain optical depth with a specific surface mass density, for example, allowing us to model plateaus that are more massive. This of course provides no information about what the “particle” properties are within the plateaus which could invalidate this conclusion. Thusfar, preliminary analyses of the autocorrelation lengths in the rings taken at face value seem to indicate that they are smaller (and thus the opacity is actually higher) in the plateaus than away from them in the low- $\tau$  regions (Colwell, priv. comm.). However, it is still unclear how to interpret this observation. It could mean, for example, that the largest particles in the plateaus may be *smaller* than the largest particles outside of the plateaus (something that would likely affect the viscosity there as well). Thus, we employ this model with the noted caveat until further analyses are conducted.

### 2.2.6 Viscosity

Apart from the angular momentum transport due to the ballistic transport process, the other non-Keplerian effect we consider in our model is viscous angular momentum transport. The inclusion of viscosity  $\nu$  as a diffusive mechanism is key in counterbalancing the sharpening effects of ballistic transport, which can be asymptotic especially near sharp edges. Under-

standing the viscosity in planetary rings continues to be an ongoing process. Well prior to Cassini, the efforts to quantify both analytically (e.g., Goldreich and Tremaine, 1978) and numerically (e.g., Wisdom and Tremaine, 1988) ring viscosity assumed ensembles of identical spheres undergoing inelastic collisions while orbiting in the gravity field of the planet. These models assumed low filling factors, particle spins and self-gravity were ignored, and the coefficient of restitution was velocity independent.

More recently, analyses of Cassini UVIS occultation data have highlighted the “clump-and-gap” structure (see above) of the rings, with the majority of the ring mass possibly hiding in the opaque clumps, while the gaps contain a lower  $\tau$  and perhaps smaller particles (e.g., Colwell et al. 2007; Nicholson et al. 2008). The observed optical depth is controlled by the relative abundance of these clumps and gaps, but the ring viscosity is controlled by the mass and dimension of the clumps and/or large particles. Local  $N$ -body simulations demonstrate that once strong wake structures form, the effective viscosity is dominated by gravitational torques due to the wake structure, because gravitational scattering by wakes increases relative random velocities which enhances the local component of the viscosity (Salo 1995; Daisaka and Ida 1999; Schmidt et al. 2009). Thus we will likely require a more robust model for the rings’ viscosity that accounts for their wake structure, in which not only physical collisions (which leads to both local and non-local transport of angular momentum), but also the effects of mutual gravitational interactions are considered (e.g., Hahn 2008).

One such model is that of Daisaka et al. (2001) which includes all of these physics and is derived from their local  $N$ -body simulations. Daisaka et al. used a limited range of surface densities  $\sigma$  to find that the dependence of the viscosity on the surface density goes as  $\sigma^2$ .

However, according to more recent dynamical simulations (Stewart et al. 2007; Robbins et al. 2009), gravity wakes in the A ring behave quite differently than they do in the B ring: while clump lifetimes are much shorter in the A ring relative to the B ring, clumps extend further in the radial direction when stretched, and the angle of the wakes relative to the azimuthal direction has a wider time variation. These differences will clearly affect the viscosity. However, this endeavor still remains problematic because, e.g., there is still no clear indication of how the magnitude of the viscosity varies radially at different points in the rings.  $N$ -body simulations indicate the possibility of drastic changes in the viscosity radially by an order of magnitude difference from 120000 km to 100000 km for the same value of  $\sigma$  (Stewart, priv. comm.). In order to apply these updated models to our BT code, we will need a more clear idea of what the relationship between  $\sigma$  and  $\tau$  with respect to  $\nu$ , and over a broad range of surface density values. Work in this area is ongoing.

For this paper, we continue to utilize the radially variable expression for the ring viscosity used by previous workers (Durisen *et al.*, 1992; 1996; Cuzzi and Estrada, 1998) which is based on the work of Wisdom and Tremaine (1988). Their calculation includes both local and nonlocal contributions to the angular momentum flux which is proportional to the viscosity in steady state. Durisen et al. (1992) provide an analytical fit to the numerical results of Wisdom and Tremaine (1988) for an ensemble of identical particles of size  $r_p$

$$\frac{3\nu}{\Omega r_p^2} = 2.5 \tau^{1.1} + \frac{1.7 \tau}{0.30 + \tau^2}, \quad (21)$$

which has an accuracy of  $\pm 5 - 10\%$  for  $0 \leq \tau \leq 2$  when compared with the numerical results. A suitable coefficient  $\Omega r_p^2/3$  was determined based on the results of simulations with

two particle sizes (e.g., Salo, 1991) that showed that the overall spreading rate of particles is determined by the largest ones. For the  $r^{-3}$  powerlaw that we use, and our fiducial lower and upper bounds  $r_1$  and  $r_2$  (Sec. 2.2.2), one finds that the bulk of the mass and 1/3 of the optical depth are due to particles with radii greater than 64.6 cm (Durisen *et al.*, 1992). Thus the exact expression for the viscosity we use in the BT code is

$$\nu(R, \tau) = 0.51 \left( \frac{\bar{r}_p}{64.6 \text{ cm}} \right)^2 \left( \frac{1.55 R_S}{R} \right)^{3/2} \left[ 1.5(\tau/3)^{1.1} + \frac{(\tau/3)}{0.30 + (\tau/3)^2} \right] \text{ cm}^2 \text{ s}^{-1}, \quad (22)$$

where  $\bar{r}_p = 64.6 \text{ cm}^2 \text{ s}^{-1}$  for the range of particle sizes chosen. Choosing different values for  $\bar{r}_p$ , which effectively amounts to changing the particle size distribution upper and lower bounds, allows us to vary the *magnitude* of the viscosity in the code. We will refer to this variation in magnitude for specific model runs through a scaling factor  $f_\nu$  which is unity for our fiducial parameters. Durisen *et al.* (1992) found that a steady state edge like that of the inner B ring can be sustained by a balance between sharpening as a result of BT with a strongly prograde ejecta distribution versus spreading due to viscous diffusion (using Eq. [22] for  $f_\nu = 1$ ) somewhat remarkably for optical depth contrasts between the low- and high- $\tau$  regions that are satisfied at both the inner A and B ring edges.

### 2.2.7 Ejecta yields and velocity distributions

In this paper, we exclusively use the longitude-averaged angular distribution and ejecta yield emission rate for non-disruptive impacts derived by Cuzzi and Durisen (1990), which is strongly biased towards the prograde (sub-Keplerian) direction. Impacts from heliocentric particles occur preferentially on the leading face of ring particles, and the cratering ejecta,

which tends to be sprayed opposite to the direction of the impact, emerges with velocities larger than the local Keplerian orbital velocity. As a result, the ejecta, now on slightly elliptical, inclined orbits having semimajor axes larger than their radius of ejection, reimpact the ring plane at a distance generally further away from the central planet than where they were ejected. Since these prograde-biased ejecta carry a smaller amount of angular momentum per unit mass than the material where they land, there is a net radial inward drift of material.

As mentioned in Section 1, the ejecta yield  $Y$  from a cratering impact depends on the hardness of the target as well as the angle of impact. The mass ejecta yields for primarily silicate material impacting icy particles has typically been taken to be in the range  $Y \approx 10^4 - 10^5$ . In the work of Cuzzi and Estrada (1998), these values were applied to the results of Lange and Ahrens (1987) to obtain their adopted value of  $Y = 3 \times 10^4$  at an impact velocity of  $14 \text{ km s}^{-1}$  for their simulations. These authors point out that their adopted values are scaled from experiments at lower impact velocities, and refer to macroscopic projectiles hitting solid icy targets, rather than micrometeorites impacting the regolith of ring particles where particles within the regolith may typically be the same size or not much bigger than the impactor. Because the problem of ring particle bombardment continues to be a more complicated process than what laboratory experiments can elucidate, we choose to use the yield as a variable parameter with a range from  $\sim 10^3 - 10^6$  which covers a full range from hard to soft, fluffy or porous targets (ANY NEWER STUFF TO REFER TO?)

Our ejecta speeds are parameterized by the unitless variable  $x \equiv v_{\text{ej}}/v_K$ , where  $v_K$  is the local circular orbit speed in the plane of the ring, and the ejecta velocities  $v_{\text{ej}}$  can range from

as small as  $1 \text{ m s}^{-1}$  to as high as  $\sim 100 \text{ m s}^{-1}$  for silicates (see, e.g., Fig. 3 of Durisen *et al.*, 1992). The ejecta velocity distribution is given by a pure power law

$$f(x) = \begin{cases} x^{-n} & x_b \leq x \leq x_t; \\ 0 & \text{otherwise.} \end{cases}, \quad (23)$$

where  $f(x) dx$  describes the fraction of ejecta mass having speeds in the interval  $x$  to  $x + dx$ , and  $x_b$ ,  $x_t$  are the adjustable lower and upper bounds of the ejecta distribution. Durisen *et al.* (1992) and Cuzzi and Estrada (1998) both adopted a value of  $n = 13/4$  which was a fit to the high-end ejecta velocities in hard target laboratory data for solid basalt (e.g., see Burns *et al.*, 1984). In this paper, we only model a pure power law for  $f(x)$ . Durisen *et al.* (1992) looked at both pure power laws as we utilize here, but also looked at a power law with a “knee” which was considered more applicable to model the hard target, higher-end speed distribution. If icy ring particles act more like sand, then a pure power law with a lower effective  $x_t$  and a slightly less steep slope ( $n = 3$ ) may be more appropriate. The main difference between the two distributions that Durisen and colleagues found was that the pure power law required higher yields to dominate viscous transport, and produced a steeper steady-state edge.

Finally, because of the improved computational ability of our parallelized BT code, we can achieve what Durisen *et al.* (1992) could not, namely to simulate large radial regions over long periods of time while simultaneously being able to resolve structure for very small  $x_b$ . Moreover, the BT code can readily be altered to adopt velocity distributions which have a more complex behavior. In future papers, we will consider this as well as isotropic

and retrograde (sub-Keplerian) dominated impact ejecta distributions (see discussion in Sec. 4) which requires that we rerun the models of Cuzzi and Durisen (1990) with altogether different sets of conditions.

### 2.2.8 Mass loading and ring torque

In our BT code, we include the direct effects of meteoroids in our simulations of the structural and compositional evolution on the rings. The direct mass deposition term is already accounted for in our ballistic transport equations through  $\dot{\sigma}_{\text{im}}$  (see, e.g., RHS of Eq. [7]). A much more important effect than the direct deposition of mass is the changes that occur to the specific angular momentum  $h$  caused by the combination of mass and angular momentum deposition. An annulus subject to these effects will drift radially adjusting its  $h$  to match that of the local orbital  $h = h_c$  with drift velocities (Durisen *et al.*, 1996; *cf.* Eq. [9])

$$v_{\text{dir}} = v_{\text{torq}} + v_{\text{masl}} = \left( \sigma \frac{dh_c}{dR} \right)^{-1} \left[ \left( \frac{\partial j}{\partial t} \right)_{\text{dir}} - h_c \dot{\sigma}_{\text{im}} \right], \quad (24)$$

where the first term in the RHS of (24) is the per-unit-area meteoroid angular momentum deposition rate. If one considers the mass deposition rate alone (second term on the RHS), the timescale for a ring to be hit by its equivalent mass is given by  $t_{\text{masl}} = \sigma / \dot{\sigma}_{\text{im}} = Y t_G$  (*cf.* Sec. 2.2.1). A comparable drift time from some radial location  $R$  to the central body due to this term would be  $\Delta R / |v_{\text{masl}}| = (\Delta R / 2R) t_{\text{masl}}$ . For typical ring parameters, it is clear that radial drifts due to the mass loading effect alone would cause the C ring and most of the B ring to be lost to Saturn faster than it would take for the accumulation of enough extrinsic material to equal the original  $\sigma$  (Durisen *et al.*, 1996).

The direct angular momentum deposition rate leads to a net negative torque on the rings. The reasons for this can be two-fold. The first is that in regions of moderate or low optical depth, micrometeorites that pass through the ring are not necessarily absorbed. Recall that the reason that the ejecta flux distribution of Cuzzi and Durisen (1990) is strongly biased in the prograde direction is due in great part to the aberrations introduced due to the motions of Saturn and of the orbits of the ring particles. Due to these aberrations the slant path of the incoming micrometeorites statistically tend to lead to more impacts on the leading face of orbiting ring particles, and these particles are more completely absorbed. A negative torque occurs because meteoroids with negative specific angular momentum are preferentially absorbed, and this would be the case even if the micrometeorite flux were isotropic (Durisen *et al.*, 1996). This effect does not affect very high optical depth regions because then all micrometeorites are absorbed. A second reason that can lead to a negative torque is if a significant amount of the ejecta escape the ring system carrying with them specific angular momentum. With very large  $Y$ , this could be a significant effect, but we do not consider this possibility currently in our models.

Durisen *et al.* (1996) used the techniques of Cuzzi and Durisen (1990, e.g., see their Fig. 15) to calculate the drift velocities due to mass loading and asymmetric micrometeoroid absorption (which causes the negative torque) as functions of optical depth for a broad range of radii and optical depths. They derived simple analytical functions of  $R$  and  $\tau$ , which we utilize in the BT code, that capture the results of their numerical calculations. The analytical fits to the drift due to direct effects are given by

$$v_r^{\text{torq}}(R, \tau) = - [1.1 \times 10^{-8}(R/R_S) + 4.0 \times 10^{-8}] e^{(-\tau/0.28)^{0.74}} \text{ cm s}^{-1}, \quad (25)$$

$$v_r^{\text{masl}}(R, \tau) = - \frac{1.1 \times 10^{-8}(R/R_S) + 6.0 \times 10^{-8}}{\tau} (1 - e^{-\tau/0.47})^{0.98} \text{ cm s}^{-1}. \quad (26)$$

In these expressions, it is implicitly assume that  $\sigma = 96 \text{ g cm}^{-2}$  for  $\tau = 1$ .

## 2.3 Numerical Methods

### 2.3.1 Stepping in time

In the BT code, the ring is divided up into  $N$  ‘ringlets’, or annuli with bin centers  $R_j$ . The annuli are treated as Lagrangian cells whose  $N + 1$  edges  $b_j$  ( $b_j < R_j < b_{j+1}$ ) drift at velocities due to a combination of the ballistic transport mechanism, and ring viscosity as given in Eq. (??). Other contributions to the radial drift due to mass loading and/or loss of ejecta momentum, or radial drifts due to torques that arise as a result of the asymmetric absorption of meteoroids (Durisen *et al.*, 1996) are also included in  $v_r$ . The main quantities of interest, the surface density  $\sigma$ , optical depth  $\tau$ , opacity  $\kappa$ , viscosity  $\nu$ , and fractional mass of pollutant  $f_e$  are evaluated at bin centers which lie midway between the moving bin edges. Given these quantities at bin center locations  $R_j^n$  at time  $t^n$  we advance the simulation

$$t^{n+1} = t^n + \Delta t^n, \quad (27)$$

using a variable timestep  $\Delta t(t)$  (see Sec. 2.3.3) as described below.

1. At the beginning of every iteration, we implement a rezoning scheme (Durisen *et*

*al.*, 1992) that searches over the radial grid to find annuli that have become narrower, or wider than preassigned limits. If the condition is found, the narrowest bin is merged with its smallest neighbor, while the largest bin is split in two. The physical quantities of a merged or split bin are adjusted accordingly. This is done to ensure that the resolution of the code remains comparable through a given simulation.

2. The viscosities  $\nu_j^n$  are updated from the last timestep  $t^n$  using our chosen viscosity law (see Sec. 2.2.6).

3. The appropriate timestep size  $\Delta t^n$  for the current iteration is determined from the stability criteria outlined in Sec. 2.3.3.

4. The losses  $\Lambda^n$  and gains  $\Gamma^n$  are determined at every  $R_j^n$ . As mentioned in Sec. 2.2.4, our method of integration uses a lookup up table for the current values of the fractional mass, the optical depth and other quantities that depend on these parameters. Thus prior to integration, the relevant quantities are interpolated onto a very fine grid. The loss and gain calculation provides the direct term changes to the ring surface density and fractional surface mass densities of extrinsic absorbing material  $\sigma_e$  and intrinsic, icy materials  $\sigma_i$  at time  $t^{n+1}$ .

5. The drift velocity due to ballistic transport at bin center  $R_j$  is calculated from Eq. (9) using the difference formula

$$(v_r^{\text{ball}})_j^n = \frac{2\sqrt{R_j}}{\sigma_j^n} \left[ \Gamma_{j,h}^n - \Lambda_{j,h}^n - \sqrt{R_j} (\Gamma_{j,m}^n - \Lambda_{j,m}^n) \right]. \quad (28)$$

6. The viscous drift velocity Eq. (10) is calculated at points midway between bin centers using the differencing

$$(v_r^{\text{visc}})_{j-1/2}^n = -\frac{3}{\bar{\sigma}_{j-1}^n \bar{R}_{j-1}^n} \frac{(\sigma\nu\sqrt{R})_j^n - (\sigma\nu\sqrt{R})_{j-1}^n}{R_j^n - R_{j-1}^n}, \quad (29)$$

where all quantities are evaluated at time  $t^n$ , and the bar represents an average of the quantity between bins  $j$  and  $j-1$ . The viscous drift velocities are then interpolated to the true bin edges which generally do not lie midway between bin centers.

7. If mass loading and ring torques are included in the simulation, then these velocities which depend on  $\tau_j^n$  are calculated at bin centers using Eqns. (26) and (25) from Sec. 2.2.8.

8. The total changes due to direct deposition terms to the ring surface mass density (RHS of Eq. [7]), as well as those to the surface mass densities of extrinsic and intrinsic materials are calculated using

$$\begin{aligned} \sigma_{j,\text{dir}}^{n+1} &= \sigma_j^n + \Delta t^n [(\dot{\sigma}_{\text{im}})_j + \Gamma_{j,\text{m}}^n - \Lambda_{j,\text{m}}^n]; \\ (\sigma_e)_{j,\text{dir}}^{n+1} &= (f_e)_j^n \sigma_j^n + \Delta t^n [\eta f_{\text{ext}} (\dot{\sigma}_{\text{im}})_j + \Delta\sigma_e]; \\ (\sigma_i)_{j,\text{dir}}^{n+1} &= [1 - (f_e)_j^n] \sigma_j^n + \Delta t^n [(1 - \eta f_{\text{ext}}) (\dot{\sigma}_{\text{im}})_j + \Delta\sigma_i] \end{aligned} \quad , \quad (30)$$

where  $\Delta\sigma_e$  and  $\Delta\sigma_i$  represent the integrals on RHS of Eqns. (11) and (12), respectively. The new fractional mass due only to direct terms is then calculated from  $(f_e)_{j,\text{dir}}^{n+1} = (\sigma_e)_{j,\text{dir}}^{n+1} / \sigma_{j,\text{dir}}^{n+1}$ .

9. Bin-centered velocity contributions to the drift velocity  $v_r$  are interpolated to bin edges, and then combined to evolve bin edges to their new  $t^{n+1}$  positions:

$$b_j^{n+1} = b_j^n + \Delta t^n (v_r)_j^n. \quad (31)$$

The new bin centers are then taken to be midway between bin edges  $R_j^{n+1} = (b_{j+1}^{n+1} + b_j^{n+1})/2$ .

10. The divergence term contribution to the surface mass density on the LHS of Eq. (7)

then is calculated from

$$\sigma_j^{n+1} = \sigma_{j,\text{dir}}^{n+1} \frac{\mathcal{A}_j^n}{\mathcal{A}_j^{n+1}}, \quad (32)$$

where  $\mathcal{A}_j^n$  and  $\mathcal{A}_j^{n+1}$  are the computed areas of the annuli  $j$  at times  $t^n$  and  $t^{n+1}$ . The inward (or outward) drift of pollutant is then taken into account by the same technique. Alternatively, if we only model the evolution of composition while keeping the ring structure fixed (as in Cuzzi and Estrada, 1998) we solve the divergence term using the method described in Sec. 2.3.2.

11. The optical depths  $\tau_j^{n+1}$  are calculated using the new values of the ring surface mass density and our chosen model for the opacity which can itself depend on the optical depth or surface density (see Sec. ???).

### 2.3.2 Tracking material of different composition exclusively

The direct term in the calculation of the fractional mass evolution is given by Equations (11) and (12), and are valid whether the underlying ring structure is evolving or not. The divergence term in these equations accounts for the ejected material from a given ring annulus that may be replaced by either inward or outward drifting material (e.g., Lissauer 1984; Durisen *et al.*, 1989;1992). In the BT code, we allow that the outward (inward) thrown material may be different from the material upon which it lands, or from the material which replaces it that is drifting inward (outward).

We are most interested in modeling the evolution of both structure and composition in

tandem; however, for robustness we would like our code to be able to explore cases in which only composition is allowed to change with time while the rings' structure remains steady state (e.g., as was the case for Cuzzi and Estrada, 1998). The technique we use to solve the divergence term though only works when the Lagrangian bins are allowed to evolve with time (due to the combined  $v_r$ ). Thus we must implement a separate subroutine to calculate the divergence term for the surface mass densities of the extrinsic and intrinsic materials that is applicable when bin centers and edges remain fixed.

In the case of only compositional evolution, the radial drift of material at each time step is determined by solving the equation

$$\frac{\partial q}{\partial t} = -\frac{1}{R} \frac{\partial}{\partial R} (Rq v_r) = -\frac{F}{R} - \frac{\partial F}{\partial R}, \quad (33)$$

where  $q = f_e \sigma = \sigma_e$ , and  $F = qv_r$ . Equation (33) is solved using a Two-Step Lax-Wendroff method (Press *et al.*, 1992) which is second order accurate in time. Normally, spatial bins in the BT code are Lagrangian annuli whose edges move at different velocities, meaning our grid spacing is always unequal. Although this is not an issue when we only model compositional evolution (bin spacing can be the same everywhere), we derive differencing formulae below so that they can be applicable to unequal spacing (and thus an evolving grid) as a means of comparison by using the Lagrange interpolation formula to find the proper differencing expression for the derivative  $\partial F/\partial R$ . The Lagrange interpolation formula for a function  $F(R)$  defined on a finite grid of points  $R_i$  can be written as

$$F(R) = \sum_{i=0}^{N_L} \frac{\lambda(R) F_i}{(R - R_i) \lambda'(R_i)}, \quad (34)$$

where  $\lambda(R) = (R - R_0)(R - R_1)\dots(R - R_{N_L})$  and the intervals  $R_{i+1} - R_i$  need not be equally spaced, and  $\lambda'$  is its derivative evaluated at  $R_i$ . We find the three point differencing formula ( $N_L = 2$ ) centered about the point  $R_j$ , and then take the derivative with respect to  $R$ . Evaluating this expression at  $R_j$  then gives the appropriate differencing formula on the interval  $[R_{j-1}, R_{j+1}]$ .

We define the flux terms  $F = qv_r$  at the intermediate timestep  $n + 1/2$  and grid positions  $j \pm 1/2$  using a Lax scheme:

$$q_{j\pm 1/2}^{n+1/2} = \frac{1}{2} (q_j^n + q_{j\pm 1}^n) - \frac{\Delta t}{2} \frac{F_{j\pm 1}^n + F_j^n}{R_{j\pm 1} + R_j} \mp \frac{\Delta t}{2h_{\pm}} (F_{j\pm 1}^n - F_j^n), \quad (35)$$

where  $h_+ = R_{j+1} - R_j$  and  $h_- = R_j - R_{j-1}$ . The above expressions are then substituted into the properly centered equation

$$q_j^{n+1} = q_j^n - \Delta t \frac{(qv_r)_{j+1/2}^{n+1/2} + (qv_r)_{j-1/2}^{n+1/2}}{2R_j} - \Delta t \left[ \frac{h_-^2 (qv_r)_{j+1/2}^{n+1/2} - h_+^2 (qv_r)_{j-1/2}^{n+1/2}}{h_+ h_- (h_+ + h_-)} \right]. \quad (36)$$

With a minor amount of algebra, Equation (36) takes the numerical form

$$\begin{aligned} q_j^{n+1} = & -\alpha_+ (v_r)_{j+1/2}^{n+1/2} (1 - \beta_+ (v_r)_{j+1}^n) q_{j+1}^n + \\ & \left[ 1 - \alpha_+ (v_r)_{j+1/2}^{n+1/2} (1 + \beta_- (v_r)_j^n) + \alpha_- (v_r)_{j-1/2}^{n+1/2} (1 - \gamma_+ (v_r)_j^n) \right] q_j^n + \\ & \alpha_- (v_r)_{j-1/2}^{n+1/2} (1 + \gamma_- (v_r)_{j-1}^n) q_{j-1}^n \end{aligned} \quad (37)$$

where the parameters  $\alpha_{\pm}$ ,  $\beta_{\pm}$ ,  $\gamma_{\pm}$  are given by

$$\alpha_{\pm} = \frac{\Delta t}{2} \left( \frac{h_+^2 + h_-^2}{h_+ h_- (h_+ + h_-)} \pm \frac{1}{2R_j} \right) \quad (38)$$

$$\beta_{\pm} = \frac{\Delta t}{h_+} \left( 1 \pm \frac{h_+}{R_{j+1} + R_j} \right), \quad \gamma_{\pm} = \frac{\Delta t}{h_-} \left( 1 \pm \frac{h_-}{R_j + R_{j-1}} \right).$$

Note that these formulae reduce to the more familiar form when  $h_+ = h_- = \Delta R$ . The intermediate timestep velocities  $(v_r)_{j\pm 1/2}^{n+1/2}$  are taken as the mean of the previous timestep, and those determined during the current timestep. In the case of no structural evolution, these velocities remain constants. Generally, the velocities  $v_r$  in the above equations are assumed to be defined at bin centers, whereas in our Lagrangian scheme they are defined at bin edges. Since we define bin centers as the mean of the bin edge locations, we do the same for the velocities in Eq. (37). Finally, the new total fractional mass that includes changes from both the direct and divergence terms is found from

$$(f_e)_j^{n+1} = \frac{(f_e)_{j,dir}^{n+1} \sigma_{j,dir}^{n+1} + \Delta q}{\sigma_j^{n+1}}, \quad (39)$$

where  $\Delta q = q_j^{n+1} - q_j^n$  is the divergence of  $f_e \sigma$ , and  $\sigma_j^{n+1}$  is the new surface density that includes both direct and divergence contributions (*cf.* Eq. [36] Cuzzi and Estrada, 1998). Of course, if structure is held fixed,  $\sigma_{j,dir}^{n+1} = \sigma_j^{n+1} = \sigma$ . We find the method above numerically stable (although see Sec. 3.1) for much larger timesteps than the code generally allows (see Sec. 2.3.3).

### 2.3.3 Time step restrictions

The structural evolution part of the BT code is explicit in nature and thus requires adherence to stability criteria. The BT code uses a variable timestep  $\Delta t(t)$  which is determined at each

step by considering several conditions. The most basic Courant condition that arises from consideration of Eq. (7) requires that

$$\Delta t \lesssim \min \left\{ \frac{2w_j}{|(v_r)_{j+1}^n + (v_r)_j^n|} \right\}, \quad (40)$$

where the bin width  $w_j = b_{j+1} - b_j$  is measured from bin edges, and an average of the total drift velocities  $v_r$  (which are also defined at bin edges) is used. The condition essentially demands that the surface density in the bin being evaluated is not receiving information from beyond the boundaries of the spatial regions defined by each grid cell. A second condition that we impose is that of the viscous Courant condition. Code stability requires that the minimum timestep be shorter than half the shortest viscous diffusion time  $t_\nu = R^2/3\nu$  across an annular cell, namely

$$\Delta t \lesssim \min \left\{ \frac{1}{2} \left[ \frac{2w_j^2}{3(\nu_{j+1} + \nu_j)} \right] \right\}, \quad (41)$$

where the viscosities  $\nu_j$  are also evaluated at bin edges. The viscous contribution to the drift velocity is present in  $v_r$ , however the stability criterion in Eq. (40) is more important when considering the inviscid case which we generally do not consider. It is a normal consequence that radial drift can cause Lagrangian bin cells to become quite narrow which can easily cause either of the above conditions to be violated and require an unreasonably small timestep. However, our rezoning scheme at every  $\Delta t$  will always prevent this (see Sec. 2.3.1).

A last condition that the BT code must adhere to is

$$\Delta t \lesssim \min \left\{ \frac{\sigma_j^n}{(\dot{\sigma}_{im})_j Y} \right\}, \quad (42)$$

which essentially states that the timestep must be less than the local gross erosion time of the ring. This obviously applies in situations where the surface density of the ring is very low (but not zero) such as near gaps or true edges. Radial cells that are empty ( $\sigma = 0$ ) are not considered in setting  $\Delta t$ . At the beginning of each loop through time, these three conditions are checked, and the new  $\Delta t$  is taken to be the minimum of these, or a default maximum timestep size which is chosen at the beginning of our simulation, generally  $\Delta t_{\max} = 0.00005 - 0.0001 t_G$ .

### 2.3.4 Numerical technique for calculating $\Lambda$ 's and $\Gamma$ 's

Numerical integration of the loss and gain integrals (Sec. 2.2.4) represent the most computationally intensive piece of the BT code. The integration over  $\theta$  is done using a  $N_\theta = 21$  point simpson rule evenly spaced in  $\cos \theta$ , while integration over  $\phi$  is done using two Gaussian quadrature points  $N_\phi$  over the azimuthal angle  $\phi = \pi/2$  to  $\pi$  (the Cuzzi and Durisen [1990] angular distribution function possesses reflection symmetry through the planes defined by  $\phi = 0$  and  $\phi = \pi/2$ , see Fig. 2, Durisen *et al.*, 1992). Since we primarily use a power-law representation of the velocity distribution (Sec. 2.2.7) the  $x$ -integration is done using a trapezoidal rule with  $N_x = 10 - 20$  quadrature points evenly spaced in  $\log x$ .

The value of the  $\theta$ -integrand at a given Simpson point is determined by interpolation over a fine grid of the values for the fractional mass, optical depth and optical depth-dependent functions. Prior to each numerical integration, we preinterpolate a much finer mesh of points

$N_{\text{mesh}} \gg N$  where the array index of the mesh is chosen to be directly proportional to radial position. This allows for integrands to be evaluated using a mesh value that is closest to the actual value of  $R$  or  $R'$  (Durisen *et al.*, 1989). This procedure somewhat mitigates the costs of doing the angular integrals which would require  $\sim N_\phi \times N_\theta \times N$  distinct searches and interpolations otherwise. Our standard value for  $N_{\text{mesh}} = 10^5$ . Use of the fine mesh provides a boost to computational speed at the expense of a small loss in accuracy.

Despite efforts to make the integrations of the losses and gains more optimal and efficient, significant improvements in speed are best achieved through parallelization of the  $\Gamma$  and  $\Lambda$  integration subroutine. This was done using the language independent communication protocol Open MPI (Message Passing Interface). The ring composed of  $N$  annuli is divided into  $n_p$  chunks, where  $n_p$  is the number of processors being utilized, with each processor executing its ‘piece’ of the loss and gain integration loops. Once completed, a communication step is called to

Since the number of operations involved in computing the loss and gain integrals scales as  $N$ , the speed up in code execution scales as  $\sim n_p$  on a single node....

Unless otherwise noted, all runs for this paper were done using eight processors in parallel...deemed sufficient for the cases we explored.

## 3 Ballistic Transport Simulations

### 3.1 Comparison to Previous Work

In this section we present some tests of the numerical code. A natural starting point for demonstrating the the new code’s utility is to reproduce the results of earlier workers. Durisen et al. (1992) modeled the relatively sharp B ring edge and its transition into a low constant optical depth “C ring” and demonstrated that the B ring inner edge (and likewise the similar inner A ring edge) can be maintained at its presently observed width through a balance between the sharpening effects of ballistic transport, and the ring viscosity’s tendency to broaden structure. Durisen and colleagues explored a range of impact yields, and ejecta speed distributions  $f(x)$  with different choices for the lower bound  $x_b$  in order to find a range over which the B ring edge could be maintained over long timescales. Here, we focus on a few specific cases choosing the same parameter values from Durisen et al. (1992).

As mentioned in Section 2.2.5, Durisen et al. scaled their models through a relationship between the mass surface density and optical depth at  $R = 1.55 R_S$  such that  $\sigma = \sigma(\tau = 1)\tau$  where  $\sigma(\tau = 1) = 96 \text{ g cm}^{-2}$ . Since in code units, the surface density is scaled by this value, plots of optical depth translate to plots of surface mass density. This scaling then represents a constant opacity model for the rings with an effective value  $\kappa = 0.104 \text{ cm}^2 \text{ g}^{-1}$ . This scaling, along with the assumption that the ring particles everywhere can be described by a  $r^{-3}$  powerlaw for particle radii between  $3 \text{ cm} \leq r \leq 3 \text{ m}$  is consistent with mostly icy ring particles with density  $1.12 \text{ g cm}^{-2}$ . Given this scaling, the initial conditions for the B

ring edge models has the optical depth (and likewise  $\sigma$ ) distribution

$$\tau(R, 0) = 0.050 + \frac{0.950}{e^{(1.52R_S - R)/D} + 1}, \quad (43)$$

where the parameter  $D = 0.0015 R_S$  which corresponds to an edge width of  $\sim 90$  km comparable to what is observed.

In **Figure 2**, we show a calculation for B ring inner edge model with  $Y = 3 \times 10^5$ , a powerlaw ejecta speed distribution with a lower bound  $x_b = 2 \times 10^{-4}$ , and a Wisdom and Tremaine viscosity with weighting factor  $f_\nu = 1$  (see Fig. 10a, Durisen *et al.*, 1992). For these choices of parameters, a gross erosion time is around 4500 years. The simulation uses a timestep of  $\Delta t = 0.0025 t_G$  and the entire run, which corresponds to a physical timescale of  $4.5 \times 10^6$  years, took 35 minutes of parallel CPU time. The black curves correspond to selected times during the evolution of the ring structure, while red curves are the corresponding fractional mass of pollutant. Over the first ten gross erosion times or so, the ring edge steepens to a roughly steady-state slope. The formation of a ramp at the base of the edge can be seen to develop between the 9  $t_G$  and 35  $t_G$  curves, becoming quite prominent by the end of the run at 99  $t_G$ . The reason for this is that there is a very high order of cancellation between direct mass exchanges and radial drifts due to ballistic transport in this region. The ramp's growth is produced by the uncanceled residual which is essentially independent of the ring viscosity there (Durisen *et al.*, 1992). Just inside the inner edge the formation of a "hump" is also observed which may likely be undulatory structure that appears for higher yields (see Fig. 4) which is more easily suppressed by viscosity for this value of  $Y$ . Also observed and shown in more detail in **Figure 3** are the undulations that emanate from the

base of the ramp. These undulations have wavelengths that are long because they are echoes of the growing ramp structure which itself is quite broad. As the ramp grows, so too does the wavelength of the low optical depth region undulations. In addition, these undulations are not so easily suppressed because the viscosity is much weaker here (*cf.* Eq. [22]).

Also plotted in Figures 2 and 3 are the fractional mass in the rings for the selected evolutionary times. Initially, the ring begins with no extrinsic pollutants ( $f_e(R, 0) = 0$ ) everywhere in the rings. Naturally, the fractional mass differences between the high optical depth B ring and low optical depth C ring are quite pronounced with a sharp transition across the B ring inner edge. However, as the simulation evolves, the differences in composition between the regions becomes less so, with the sharpness of the transition smearing out over time due to advective effects, an effect found by Cuzzi and Estrada (1998) in their compositional evolutions. The contrast though between low- and high- $\tau$  regions is muted somewhat by the choice of a constant  $\kappa$  across the rings. The Cuzzi and Estrada (1998) profile for the opacity given in Eq. (19) would produce higher contrast though its simple form cannot be applied to the structurally evolving models because it relies on a fixed position for the edge. In Figure 3 the most notable thing to notice is that the relative position of the decrease in fractional mass begins further inward in the ring with time. This would seem to suggest that the rings are brightening more and more inward with time, but this rather reflects that darkening is occurring less quickly as the ramp grows in mass (and radial extent) relative to regions inside of it.

In **Figure 4**, we reproduce a compilation of simulations over  $104 t_G$  for the B ring edge model for various combinations of  $Y$  and  $x_b$  (*cf.* Durisen *et al.*, 1992, Fig. 15). The dashed

curve corresponds to the case for  $Y = 3 \times 10^5$  presented previously with the run extended for five more gross erosion times. The dotted and solid curves represent cases with yields of  $Y = 1 \times 10^6$  and  $2 \times 10^6$ , respectively, and a lower bound in the velocity distribution of  $x_b = 1 \times 10^{-4}$  which corresponds to a velocity of  $\sim 2 \text{ m s}^{-1}$ . These runs have also have the number of bins increased to 1500 versus the 1000 used in the  $Y = 3 \times 10^5$  case, as was done in Durisen et al. (1992). Also plotted in Figure 4 is the optical depth profile obtained with Cassini from the Alpha Arae occultation (Rev 032) for comparison. The main difference between the two latter cases is that the  $Y = 1 \times 10^6$  case achieves a steady-state sharpness with an absence of high- $\tau$  undulations, while increasing the yield by a factor of two quite readily produces nonlinear growth of undulations in the inner B ring. The corresponding red curves are the fractional masses for each run. The highest yield case has the least amount of darkening which may seem counter-intuitive, but this is because the exposure time is much shorter. For the higher yield runs, the physical timescale for exposure is  $1.4 \times 10^6$  and  $6.8 \times 10^5$  years, respectively.

From the standpoint of structural evolution, we find no qualitative differences between our simulations and those of Durisen et al. (1992). The differences that do appear upon close inspection of our simulations and those of Durisen et al. may be due mostly to order  $x^2$  errors which would be most prominent near the sharp edge. We note that the simulations of Durisen et al. (1989;1992) used an erroneous expression for the angular momentum of an ejectum  $h$  that propagated to the expression for the function  $A(x, \theta, \phi)$  (see Sec. 2.2.4) used in their code (Durisen *et al.*, 1996). Here we use the corrected expression for  $A$  that is derived using the appropriate  $h$ . Furthermore, we found that the cited timestep size used

by Durisen et al. ( $\Delta t = 0.0025 t_G$ ) was too large, especially for the highest yield case. These runs were done with a timestep of  $\Delta t = 0.0002 t_G$  which is at the upper end of what we generally choose for our models. Thus, for example, the  $Y = 2 \times 10^6$  case took  $\sim 300 - 400$  minutes of dedicated parallel CPU time.

## 4 Conclusions and Future Work

*Isotropic and Retrograde Distributions.* Disruptive collisions tend to fragment the target ring particle into many pieces, leading to ejecta distribution that differs from the non-disruptive (cratering) case in terms of yield, velocities and directionality. In the cratering case, yields are large compared to the impactor, but represent a relatively small fraction of the target mass. In the disruptive case, the “yield” may consist of most (or even all) of the target particle with most of the mass located in the largest fragments (e.g., Nakamura and Fujiwara 1991). Since most of the kinetic energy is carried away by a very small amount of mass moving away at high speeds (Benz and Asphaug 1999), most of the ejecta mass moves at smaller velocities than in the non-disruptive case, with the largest fragments having the lowest velocities. Lower relative velocities imply that the throw distances of most material in the disruptive case is much smaller. Also, unlike the non-disruptive case where the cratering impact tends to “nudge” the ring particle while ejecta is backscattered (into the super-Keplerian direction), the disruptive particle ejecta may mostly forward scatter (Paolicchi et al. 1989) if the impactor-to-target ratio is sufficiently large enough to alter the momentum of the target. If so, this would tend to potentially lead to ejecta orbital velocities that are

*less* than the local Keplerian speed. Thus a considerable fraction of disruptive collisions could result in ejecta distributions in which a significant fraction of the mass may land at radii inwards of their ejection point. Projectiles which only marginally disrupt may only result in an isotropic velocity distribution (Nakamura and Fujiwara 1991). Even this would have a significantly different angular distribution than the super-Keplerian distribution now assumed.

This combination of effects allows the sub-Keplerian or isotropic ejecta to play a significant role in evolving *local* ring structure. For example, the linearity of the “ramp” features seen at the B/C and A/Cassini division boundaries can be adequately accounted for by strongly prograde ejecta with relatively low yields and high ejection velocities (Durisen et al. 1989; 1992; CE98). However, the sharpness of the inner B ring edge and the development of undulations just outside the edge suggest a component with considerably higher yields and lower ejection velocities that can be associated with disruptive impacts (Durisen, private comm. 2008). Durisen et al. (1992) speculate that a suitable combination of both distributions can be used to better match the observed optical depth features in the inner B rings (and presumably in other regions of the rings as well such as the inner A ring edge).

One other example of where the difference between super- and sub-Keplerian velocity distributions may be important can be seen in the C ring plateaus (Fig. 1). The characteristic outward-increasing slope in  $\tau$  seen in all the plateaus outside of 87500 km is a well known signature of BT due to prograde ejecta. Sub-Keplerian (or even isotropic) ejecta would lead to the opposite (or flattened) trend, which is seen in all the plateaus inside of 87500 km. An observation suggesting that disruptive impacts may be playing a role is recent Cassini Radio

Science (RSS) data that imply there are fewer  $\sim 1 - 3$  cm-sized particles in the plateaus than outside the plateaus (Marouf et al. 2008; Cuzzi et al. 2009). This is significant because  $\sim 1$  cm particles may be the size most easily disrupted by meteoroid bombardment, if the peak in the micrometeoroid flux mass distribution indeed occurs around a radius of  $\sim 100$ . One can crudely estimate the ratio of the mass of the largest fragment to the original target mass  $f_b \sim \mu Q_*/v_{\text{im}}^2$  (e.g., Melosh, 1989) where  $\mu \sim 10^6$  is the target/impactor mass ratio, and  $Q_* \sim 10^6$  ergs  $\text{g}^{-1}$  (e.g., Stewart and Leinhardt 2009) is the fragmentation energy per unit mass. Including gravitational focusing, the impact velocity  $v_{\text{im}} \sim 30$  km  $\text{s}^{-1}$  in the C ring, giving  $f_b \sim 0.1$ , well within the regime of catastrophic breakup. If so, the implication is that disruptive impacts may occur more prominently in the regions away from the plateaus.

Finally, recent work that uses the results of New Horizons to estimate the flux of EKB dust at Saturn suggests that this may be an equally important source of extrinsic material (Poppe et al., 2010, Poppe and Horányi, 2012). Furthermore, though the mass peak for this population (a few microns) is likely too small to lead to disruptive impacts, these authors' models indicate that the ejecta distributions produced from EKB dust grain impacts could likely be more isotropic (Poppe, priv. comm. 2012) providing another important element to our BT models.

## References

- BURNS, J. A., SHOWALTER, M. R., AND MORFILL, G. E., 1984. In *Planetary Rings*, (Greenberg, R., and Brahic, A., eds.), Univ. of Arizona Press, Tucson, pp ??-??.
- CHARNOZ, S., DONES, L., ESPOSITO, L. W., ESTRADA, P. R., AND HEDMAN, M. M., 2009. Origin and Evolution of Saturn's Ring System. In *Saturn from Cassini-Huygens*, (Dougherty, M. K., Esposito, L. W., and Krimigis, S. M., eds.), Springer-Verlag Press, pp. 537-576.
- CLARK, R. N., CRUIKSHANK, D. P., JAUMANN, R., BROWN, R. H., STEPHAN, K., DALLE ORE, C. M., ERIC, L. K., PEARSON, N., CURCHIN, J. M., HOEFEN, T. M., BURATTI, B. J., FILACCHIONE, G., BAINES, K. H., AND NICHOLSON, P. D., 2012. The Surface Composition of Iapetus: Mapping Results from Cassini VIMS. *Icarus* **218**, 831-860..
- COLWELL, J. E., ESPOSITO, L. W., AND SREMČEVIĆ, M., 2006. Self-gravity wakes in Saturn's A ring measured by stellar occultations from Cassini. *Geophys. Res. Lett.* **33**, L07201.
- COLWELL, J. E., ESPOSITO, L. W., SREMČEVIĆ, M., STEWART, G. R., AND MCCLINTOCK, W. E., 2007. Self-gravity wakes and radial structure of Saturn's B ring. *Icarus* **190**, 127-144.
- CUZZI, J. N., DURISEN, R. H., BURNS, J. A., AND HAMILL, P., 1979. The Vertical Structure and Thickness of Saturn's Rings. *Icarus* **38**, 54-68.
- CUZZI, J. N., LISSAUER, J. J., ESPOSITO, L. W., HOLBERG, J. B., MAROUF, E. A., TYLER, G. L, AND BOISCHOT, A., 1984. Saturn's Rings: Properties and Processes. In *Planetary Rings*, (Greenberg, R., and Brahic, A., eds.), Univ. of Arizona Press, Tucson, pp. 73-199.
- CUZZI, J. N., AND DURISEN, R. H., 1990. Meteoroid Bombardment of Planetary Rings; General Formulation and Effects of Oort Cloud Projectiles. *Icarus* **84**, 467-501.

- CUZZI, J. N., CLARK, R., FILACCHIONE, G., FRENCH, R., JOHNSON, R., MAROUF, E., AND SPILKER, L., 2009. Ring particle composition and size distribution. In *Saturn From Cassini-Huygens*, (Dougherty, M. K., Esposito, L. W., and Krimigis, S. M., eds.), Springer-Verlag Press, pp. 459-510.
- CUZZI, J. N., AND ESTRADA, P. R., 1998. Compositional Evolution of Saturn's Rings Due to Meteoroid Bombardment. *Icarus* **132**, 1-35.
- DAISAKA, H., AND IDA, S., 1999. Spatial structure and coherent motion in dense planetary rings induced by self-gravitational instability. *Earth, Plan., and Spa.* **51**, 1195-1213.
- DAISAKA, H., TANAKA, H., AND IDA, S., 2001. Viscosity in a dense planetary ring with self-gravitating particles. *Icarus* **154**, 296-312.
- DOYLE, L. R., DONES, L., AND CUZZI, J. N., 1989. Radiative Transfer Modeling of Saturn's Outer B Ring. *Icarus* **80**, 104-135.
- DURISEN, R. H., 1984A. Transport Effects Due to Particle Erosion Mechanisms. In *Planetary Rings*, (Greenberg, R., and Brahic, A., eds.), Univ. of Arizona Press, Tucson, pp. 416-446.
- DURISEN, R. H., 1984B. Particle Erosion Mechanisms and Mass Redistribution in Saturn's Rings. *Adv. Space Res.* **4**, 13-19.
- DURISEN, R. H., CRAMER, N. L., MURPHY, B. W., CUZZI, J. N., MULLIKIN, T. L., CEDERBLOOM, S. E., 1989. Ballistic Transport in Planetary Ring Systems due to Particle Erosion Mechanisms. I. Theory, Numerical Methods, and Illustrative Examples. *Icarus* **80**, 136-166.

- DURISEN, R. H., BODE, P. W., CUZZI, J. N., CEDERBLOOM, S. E., AND MURPHY, B. W., 1992. Ballistic Transport in Planetary Ring Systems due to Particle Erosion Mechanisms. II. Theoretical Models for Saturn's A- and B-Ring Inner Edges. *Icarus* **100**, 364-393.
- DURISEN, R. H., 1995. An Instability in Planetary Rings Due to Ballistic Transport. *Icarus* **115**, 66-85.
- DURISEN, R. H., BODE, P. W., DYCK, S. G., CUZZI, J. N., DULL, J. D., AND WHITE II, J. C., 1996. Ballistic Transport in Planetary Ring Systems due to Particle Erosion Mechanisms. III. Torques and Mass Loading by Meteoroid Impacts. *Icarus* **124**, 220-236.
- ELLIOTT, J. P., AND ESPOSITO, L. W., 2011. Regolith Depth Growth on an Icy Body Orbiting Saturn and Evolution of Bidirectional Reflectance due to Surface Composition Changes. *Icarus* **212**, 268-274.
- ESPOSITO, L. W., 1987. Structure and Evolution of Saturn's Rings. *Icarus* **67**, 345-357.
- ESPOSITO, L. W., COLWELL, J. E., LARSEN, K., MCCLINTOCK, W. E., STEWART, A. I. F., TEW HALLETT, J., SHEMANSKY, D. E., AJELLO, J. M., HANSEN, C. J., HENDRIX, A. R., WEST, R. A., KELLER, H. U., KORTH, A., PRYOR, W. R., REULKE, R., AND YUNG, Y., 2005. Ultraviolet Imaging Spectroscopy Shows an Active Saturnian System. *Science* **307**, 1251-1255.
- ESTRADA, P. R., AND CUZZI, J. N., 1996. Voyager Observations of the Color of Saturn's Rings. *Icarus* **122**, 251-272.
- ESTRADA, P. R., CUZZI, J. N., AND SHOWALTER, M. R., 2003. Voyager Color Photometry of Saturn's Main Rings: A Correction. *Icarus* **166**, 212-222.

- ESTRADA, P. R., AND DURISEN, R. H., 2011. Modeling the Long Term Evolution of the C Ring due to Meteoroid Bombardment. Proceedings of the Rings 2011 Workshop, Ithaca, NY.
- GOLDREICH, P., AND TREMAINE, S., 1978. The Velocity Dispersion in Saturn's Rings. *Icarus* **34**, 227-239.
- GOLDREICH, P., AND TREMAINE, S., 1982. Dynamics of Planetary Rings. *Ann. Rev. Astron. Astrophys.* **20**, 249-283.
- GRÜN, E., ZOOK, H. A., FECHTIG, H., AND GIESE, R. H., 1985. Collisional Balance of the Meteoroid Complex. *Icarus* **62**, 244-272.
- HAHN, J. M. 2008. The secular evolution of a close ring-satellite system: the excitation of spiral density waves at a nearby gap edge. *Astrophys. J.* **680**, 1569-1581.
- HARTMANN, W. K., 1985. Impact Experiments. 1. Ejecta Velocity Distributions and Related Results from Regolith Targets. *Icarus* **35**, 1-26.
- HEDMAN, M. M., NICHOLSON, P. D., SALO, H., WALLIS, B. D., BURATTI, B. J., BAINES, K. H., BROWN, R. H., AND CLARK, R. N., 2007. Self-gravity wake structures in Saturn's A ring revealed by Cassini VIMS. *Astron. J.* **133**, 2624-2629.
- IP, W.-H., 1983. Collisional Interactions of Ring Particles: Ballistic Transport Process. *Icarus* **54**, 253-262.
- LANDGRAF, M., BAGGALEY, W. J., GRÜN, E., KRÜGER, H., AND LINKERT, G., 2000. Aspects of the Mass Distribution of Interstellar Dust Grains in the Solar System from In-situ Measurements. *J. Geophys. Res.* **105**, 10343-10352.

- LANGE, M. A., AND AHRENS, T. J., 1982. Impact Cratering in Ice and in Ice-silicate Targets. *Lunar Planet. Sci.* **13**, 530-531.
- LANGE, M. A., AND AHRENS, T. J., 1987. Impact Experiments in Low-temperature Ice. *Icarus* **69**, 506-518.
- LISSAUER, J. J., AND CUZZI, J. N., 1982. Resonances in Saturn's Rings. *Astron. J.* **87**, 1051-1058.
- LISSAUER, J. J., 1984. Ballistic Transport in Saturn's Rings: An Analytic Theory. *Icarus* **57**, 63-71.
- LISSAUER, J. J., AND CUZZI, J. N., 1985. Rings and Moons - Clues to Understanding the Solar Nebula. In *Protostars and Planets*, (Black, D., and Matthews, M. S., eds.), Univ. of Arizona Press, Tucson, pp. ???-???
- MAROUF, E. A., FRENCH, R. C., RAPPAPORT, N., MCGHEE, C., WONG, K., THOMPSON, F., AND ANABTAWI, A., 2008. Structure and physical properties of Saturn's rings from Cassini radio occultations. Proceedings of the "Saturn After Cassini/Huygens" meeting, held at Imperial College, London, July 28 - August 1, 2008.
- MELOSH, H. J., 1989. Impact Cratering: A Geological Process. Oxford Univ. Press, New York.
- MORFILL, G. E., FECHTIG, H., GRÜN, E., AND GOERTZ, C., 1983. Some Consequences of Meteoroid Bombardment of Saturn's Rings. *Icarus* **55**, 439-447.
- NAKAMURA, A., AND FUJIWARA, A., 1991. Velocity distributions of fragments formed in a simulated collisional disruption. *Icarus* **92**, 132-146.

- NICHOLSON, P. D., HEDMAN, M. M., CLARK, R. N., SHOWALTER, M. R., CRUIKSHANK, D. P., CUZZI, J. N., FILACCHIONE, G., CAPACCIONI, F., CERRONI, P., HANSEN, G. B., SICARDY, B., DROSSART, P., BROWN, R. H., BURATTI, B. J., BAINES, K. H., AND CORADINI, A., 2008. A close look at Saturn's rings with Cassini VIMS. *Icarus* **193**, 182-212.
- NORTHROP, T. G., AND CONNERNEY, J. E. P., 1987. A Micrometeorite Erosion Model and the Age of Saturn's Rings. *Icarus* **70**, 124-137.
- OHTSUKI, K., AND EMORI, H., 2000. Local  $N$ -body simulations for the distribution and evolution of particle velocities in planetary rings. *Astron. J.* **119**, 403-416.
- POPPE, A., JAMES, D., JACOBMEYER, B., AND HORÁNYI M., 2010. First results from the Venetia Burney Student Dust Counter on the New Horizons mission. *Geophys. Res. Lett.* **37**, L11101-L11106.
- POPPE, A., AND HORÁNYI, M., 2012. On the Edgeworth-Kuiper belt dust flux at Saturn. 43rd LPSC Meeting, abstract no. 1365.
- POULET, F., AND SICARDY, B., 2001. Dynamical Evolution of the Prometheus-Pandora System. *Mon. Not. Roy. Astron. Soc.* **322**, 343-355.
- PRESS, W. H., FLANNERY, B. P., TEUKOLSKY, S. A., AND VETTERLING, W. T., 1992. Numerical Recipes in Fortran. Cambridge University Press.
- ROBBINS, S. J., STEWART, G. R., LEWIS, M. C., COLWELL, J. E., AND SREMČEVÍČ, M., 2010. Estimating the Masses of Saturn's A and B Rings from High-optical Depth  $N$ -body Simulations and Stellar Occultations. *Icarus* **206**, 431-445.
- SALO, H., 1991. Numerical Simulations of Dense Collisional Systems. *Icarus* **90**, 254-270.

- SALO, H., 1995. Simulations of dense planetary rings. III. Self-gravitating identical particles. *Icarus* **117**, 287-312.
- SCHMIDT, J., OHTSUKI, K., RAPPAPORT, N., SALO, H., AND SPAHN, F., 2009. Dynamics of Saturn's dense rings. In *Saturn After Cassini-Huygens*, (Dougherty, M. K, Esposito, L. W., and Krimigis, S. M., eds.), Springer-Verlag Press, pp.413-458.
- SHOWALTER, M. R. AND NICHOLSON, P. D., 1990. Saturn's rings through a microscope - Particle size constraints from the Voyager PPS scan. *Icarus* **87**, 285-306.
- SREMČEVIĆ, M., KRIVOV, A. V., KRÜGER, H., AND SPAHN, F., 2005. Impact-generated Dust Clouds Around Planetary Satellites: Model Versus Galileo Data. *Plan. Space Sci.* **53**, 625-641.
- STEWART, G. R., ROBBINS, S. J., AND COLWELL, J. E., 2007. Evidence for a primordial origin of Saturn's rings. 39th DPS meeting, abstract no. 7.06.
- STEWART, S. T., AND LEINHARDT, Z. M., 2009. Velocity-dependent catastrophic disruption criteria for planetesimals. *Astrophys. J. Lett.* **691**, L133-L137.
- WISDOM, J., AND TREMAINE, S., 1988. Local simulations of planetary rings. *Astron. J.* **95**, 925-940.
- ZEBKER, H. A., MAROUF, E. A., AND TYLER, G. L., 1985. Saturn's Rings - Particle Size Distributions for Thin Layer Model. *Icarus* **64**, 531-548.

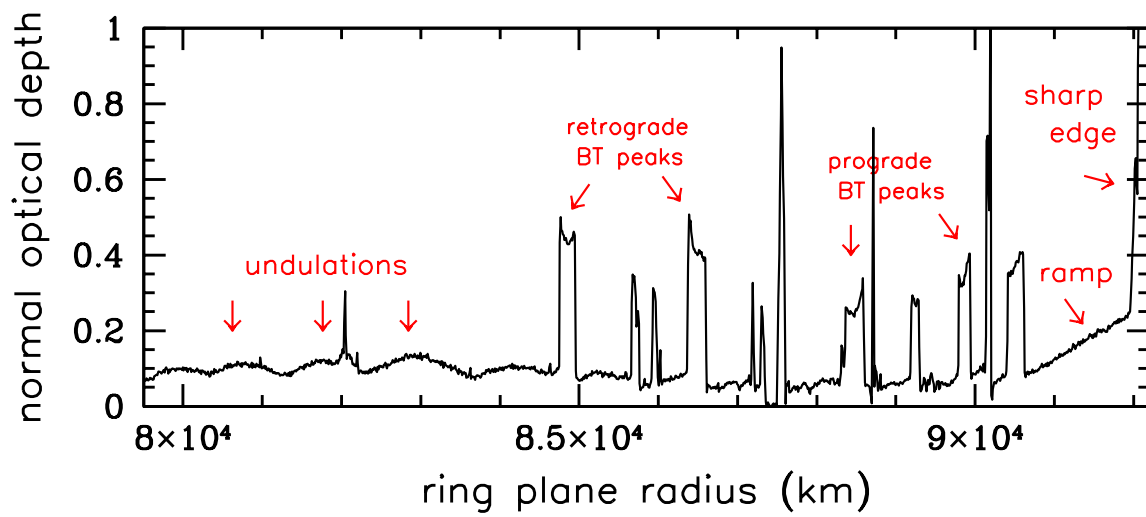


Figure 1: blah blah blah

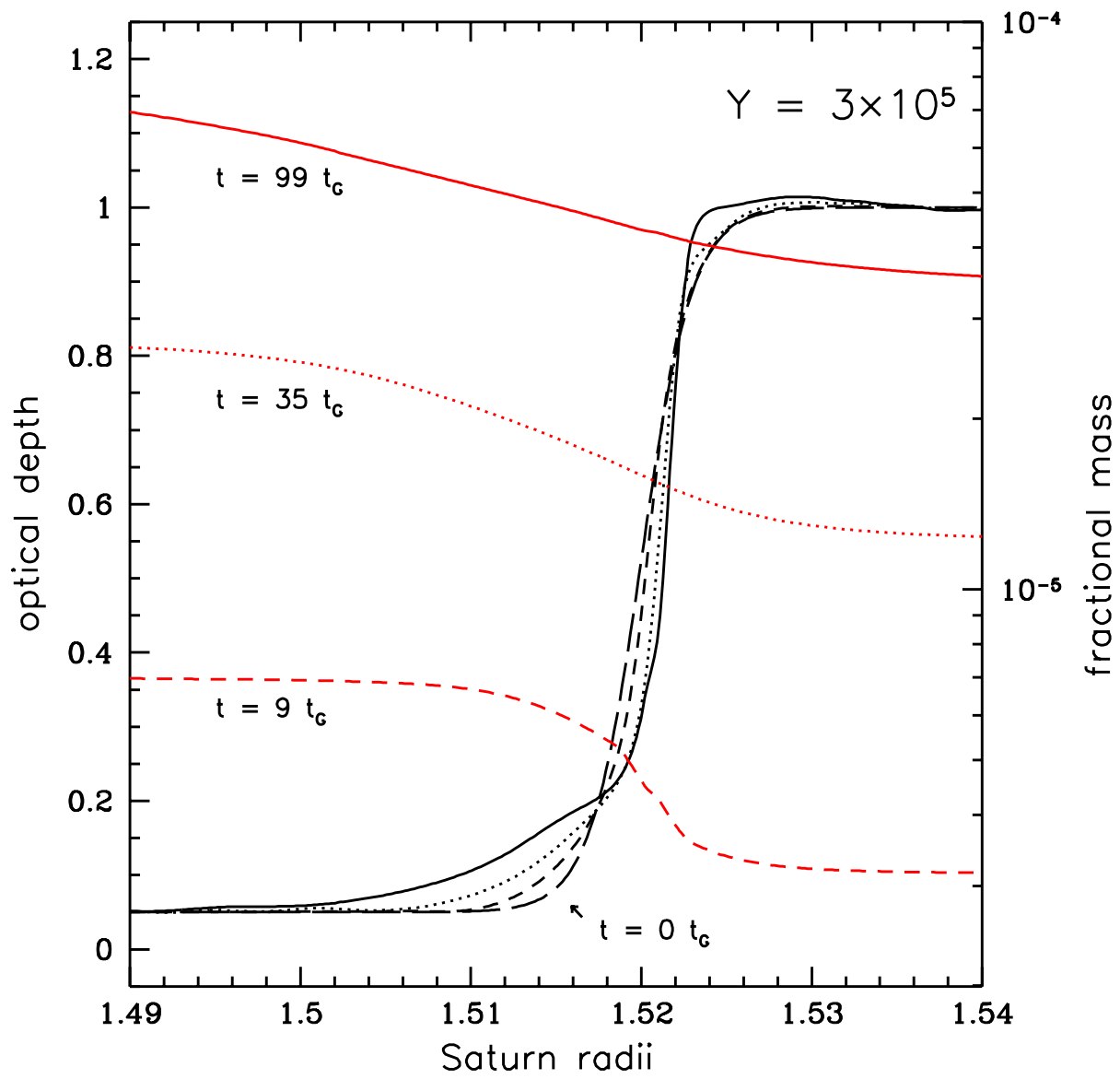


Figure 2: blah blah blah

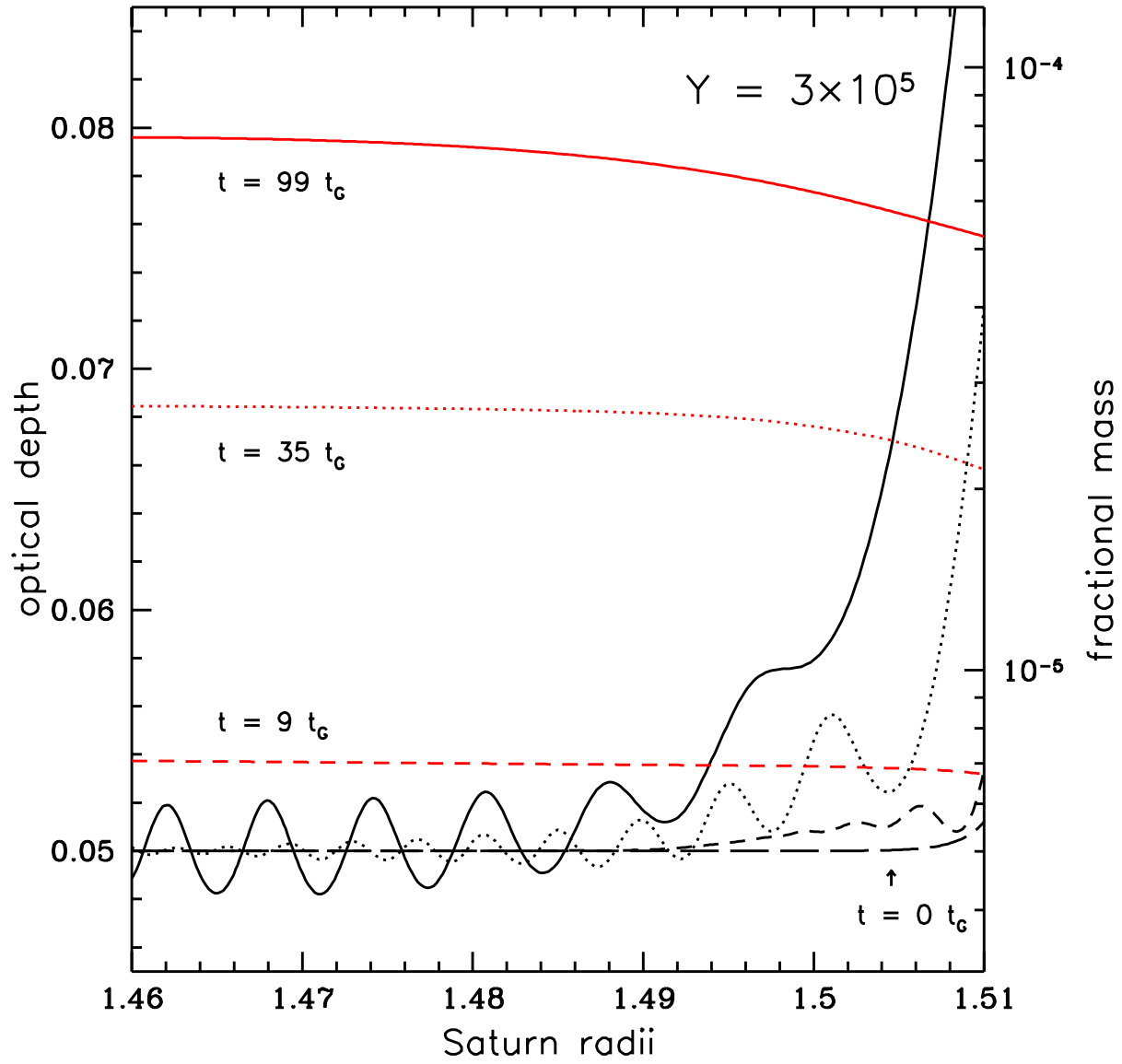


Figure 3: blah blah blah

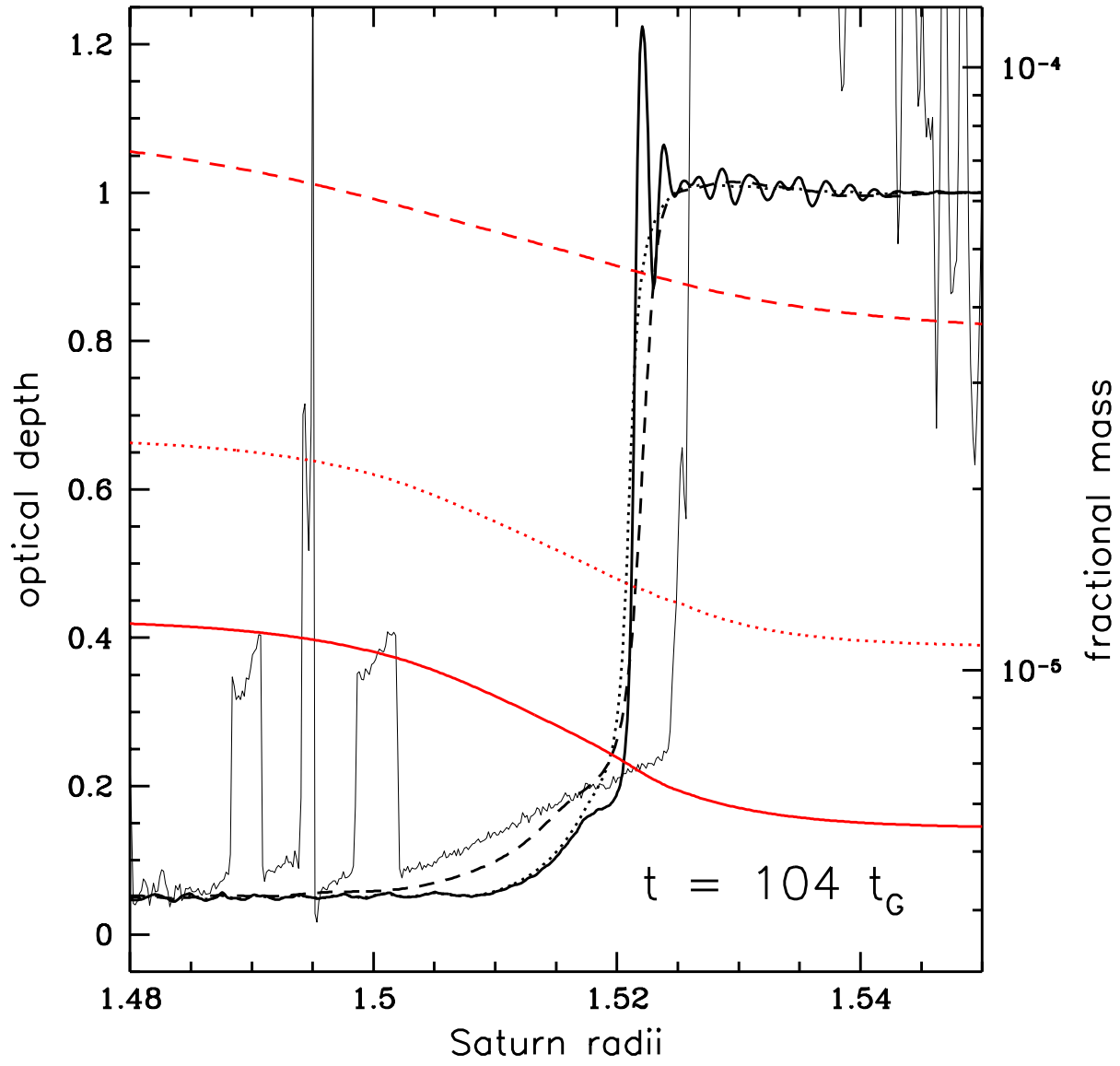


Figure 4: blah blah blah

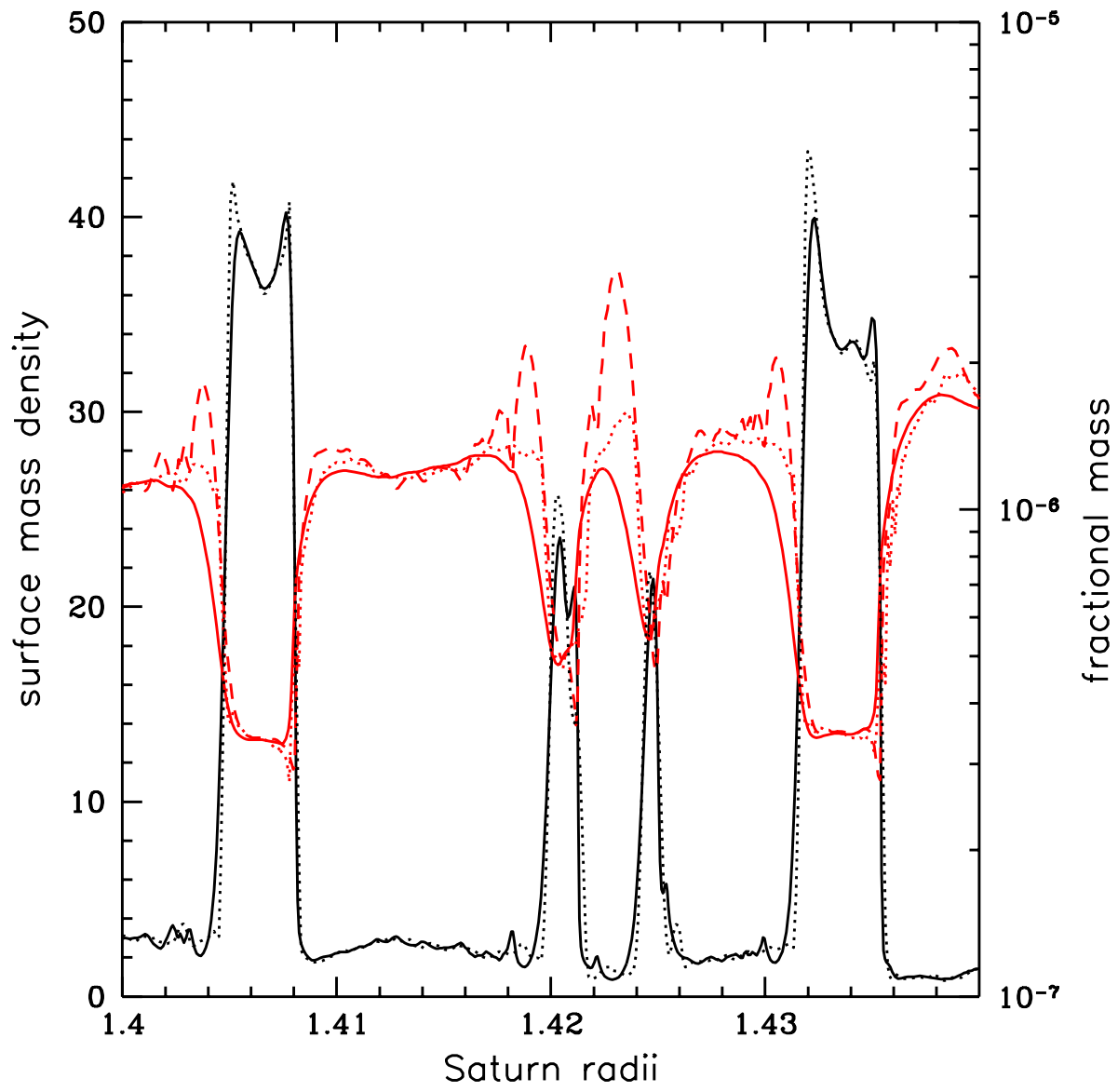


Figure 5: blah blah blah